ANUL L **2005**

S T U D I A

UNIVERSITATIS BABEŞ–BOLYAI

PHYSICA

1

EDITORIAL OFFICE: Republicii no. 24, 400015 Cluj-Napoca ♦ Phone 0264-40.53.52

CONTENTS

STUDIA UNIVERSITATIS BABEŞ BOLYAI, PHYSICA, L, 1, 2005

VIBRATIONAL SPECTROSCOPY, SURFACE-ENHANCED RAMAN SPECTROSCOPY AND THEORETICAL STUDIES OF SODIUM SALT OF 3-AMINO-3-[(5-BENZOTHIAZOLE-2YL)-FURAN-2YL]-PROPANOIC ACID

T. ILIESCU[1], D. MANIU[1], V. CHIS[1], M. TOSA[2], F. IRIMIE[2]

[1]Babes-Bolyai University, Physics Faculty, Cluj-Napoca, Romania
[2]Babes-Bolyai University, Chemistry and Chemical Engineering Faculty, Cluj-Napoca, Romania

ABSTRACT. Raman and surface–enhanced Raman spectroscopy (SERS) have been applied to the vibrational characterization of sodiu salt of 3-amino-3-[(5-benzothiazole-2yl)-furan-2yl]-propanoic acid (salt 1). Theoretical calculation (DFT) have been performed to find the optimized structure and computed vibrational wavenumbers of this salt. SER spectrum in silver colloid at pH value of 8 have been also recorded and analysed. Good SER spectrum have been obtaining, providing the chemisorption of salt 1 molecule on the silver surface. At the investigated pH value the carboxylate anion has been bonded to the silver surface through π electron system having the tilted close to flat orientation with respect to silver surface. Phenyl, thiazole and furan rings have also close to flat orientation to the metallic surface.

Introduction

Although of less importance than their α-analogues, β-amino acids are also present in peptides and different heterocycles, and their free forms and derivatives exhibit interesting pharmacological effects.

Besides their own pharmacological activity, the β-amino acids can be used as building blocks for the preparation of modified (non-natural) analogues of biological active peptides. By insertion of an β-amino acids in plane of an α-amino acid of naturally occurring pharmacologically active peptides, the activity or the effects can be modified [1]. By means of such an exchange the stability of the natural peptides can be increased since β-peptides are resistant to enzymatic degradation [2]. On the other hand, cyclic β-amino acids can by used as starting pharmacons for the synthesis of natural products or analogues and also as building blocks in drugs research [1]. Because of the natural occurrence and the biological activity, interest in physico-chemical investigation of the β-amino acids and their salts has rapidly increased.

The chemical aspects of the drug action, as our derivatives, are very complicated. The ideal situation is when the drug rest in non-modified form until it reach the receiving center specific of certain human organ. Receiving center can be an aria in which the drug is adsorbed with different parts of the drug molecule [3].

In this sense silver surface can be considered as artificial biological interface for drugs adsorption [4]. Certainly the adsorption on the silver surface do not resolve the very complicated problem of drug action in human body but can offer a general idea about the adsorption posibilities.

The knowledge about the structure of β-amino acids and their salts is essential for understanding their pharmacological action. Vibrational spectroscopy offers a good tool in this sense.

β-Amino acids, like its α-analogues, present in their structure near neutral and weak alkaline environments, NH_3^+ and COO^- groups. In order to understand the action of these groups on the vibrational spectrum we select sodium salt of an amino acid in which NH_2 and COO^-groups are present.

In the first part of this paper we present the vibrational analysis of sodium salt of 3-amin-3-[5-benzothazole-2yl)-furan-2yl]-propanoic acid (salt 1) from experimental (Raman) and theoretical (DFT calculations) point of view.

The adsorption study on silver surface of salt 1 specie in order to establish the nature and its orientation on metal surfaces is the contribution of the second part of this work.

The salt 1 molecular structure is presented in Fig. 1.

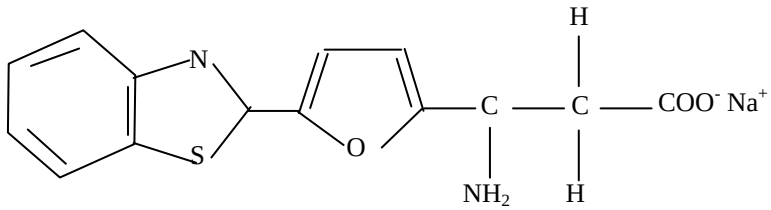

Fig. 1. General structure of sodium salt of 3-amino-3-[(5-benzothiazole-2yl)-furan-2yl]-propropanoic acid

Experimental

Sample and instrumentation

3-amino-3-[5-benzothiazole-2yl)-furan –2yl]-propanoic acid was prepared starting from corresponding aldehyde using the Rodionov method [5]. Sodium salt of this β-amino acid was prepared by addition of NaOH.

FT-Raman solid state spectrum was recorded using Brüker IFS 120HR spectrometer with integrated FRA 106 module and resolution of 2 cm^{-1}. Radiation of 1064 nm from Nd-YAG laser was employed for Raman spectrum excitation. 180^0 geometry was used to collect the scattered light.

Surface enhanced Raman spectrum (SERS) was performed on a Dilor Labram system equipped with an Olympus LMPlan FI 50 microscope obiective, an

1800 lines/mm grating and an external laser with an emission wavelength of 514.5 nm. In the recording of the micro-Raman spectra a power of 100 mW on the sample has been employed. 180^0 geometry was used to collect the scattered light.

Sodium citrate silver colloid was prepared according the literature [6]. A small amount of 10^{-2} mol/L salt 1 aqueous solution was added to 0.6 mL colloid. 0.1 mL 10^{-1} mol/L NaCl solution was added to obtain coagulation of the sol. The final concentration of the sample 1.4 10^{-3} mol/L and pH value of 8 was obtained. All measurements were performed at room temperature.

Computational details

The molecular geometry optimization and vibrational frequencies calculation were performed with the Gaussian 98 W [7] by using semiempirical (PM3) [8], (AM1) [9] and DFT methods. In the last case the combination of the B3 [10] exchange functional of LYP [11] correlation functional is used. The split valence-shell G-31 G(d) basis set of the Pople's group [12], augmented by d polarization functions on havy atoms has been used in conjunction with DFT method. All the calculation has been carried out with the restricted closed-shell formalism.

The geometry was fully optimized without any constraint with the help of analytical gradient procedure implemented with Gaussian 98 W program. The force constants were calculated by analytical differentiation algorithm for each completely optimized geometry. Prior to compare the calculated vibrational frequencies with the experimental counterparts the former have been scaled by appropriate scaling factor recommended by Scot and Radom [13]. For DFT method at B3LYP/6-31G(d) level, the recommended frequency scaling factor for high and low frequencies are 0.96414 and 1.0013 respectively. Vibrational mode assignments were made by visual inspection of modes animated by using Molekel program [14].

Results and discussion

A. Theoretical calculation

Fig. 2 presents the optimized geometry of salt 1 obtained by DFT theoretical calculation using B3LYP/6-31G(d) level of theory.

As can be seen in Fig. 2, phenyl , thiazole and furan rings are in the same plane. This plane contain too the COO^- group and the C15C26 bond. The C5C15N16 and C5C15C17 angles are biger than 90^0 (see Fig 2 for the atoms number).

Theoretical calculation allow to obtain the assignment of vibrational modes. Table 1 presents the calculated scaled frequencies, corresponding experimental FT Raman data and assignment of the vibrational modes of salt 1 molecule.

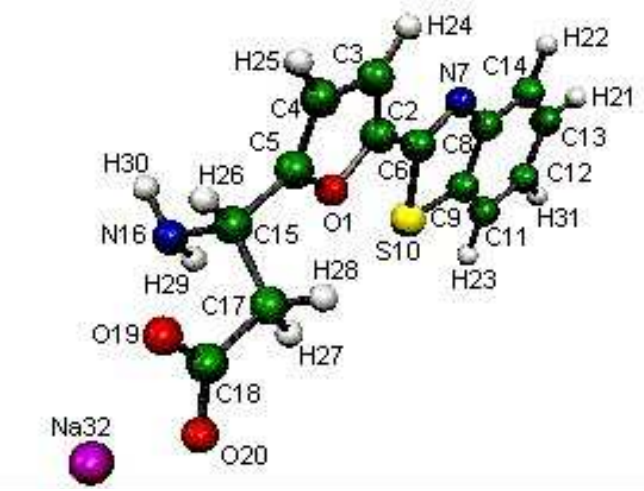

Fig. 2. Optimized geometry of sodium salt of 3-amino-3-[(5-benzothiazole-2yl)-furan-2yl]-propanoic acid at the B3LYP/6-31 G(d) level of theory. Phenyl, thiazole and furan rings form a plane which contain the COO^- group.

Table 1

Experimental FT-Raman and calculated (cm^{-1}) of sodium salt of 3-amino-3-[(5-benzothiazole-2yl)-furan-2yl]-propanoic acid.

FT Raman	Frecq B3LYP (6-31Gd)	Assignment
	199	ring 1,2,3 out of plane def. (m)
	237	NH2 ρ(s), CH2 ρ (m), C15-C17-C18 δ (m)
	263	NH2 τ vs)
	276	NH2 ρ (s), CH2 ρ(m), COO^- ρ (w)
	292	NH2 ρ (s), CH ring 3 in plane def. m)
310 (vw)	318	NH2 ω (w), ring 1,2,3 out of plane def. (m)
	327	O1-C2-C6 δ (m), C9-C10 ν (w), NH2 τ (w), CH2 ρ (w)
362 (vw)	354	NH2 τ (m), CH2 ω (m), CH ring 3 in plane def. (w)
390 (vw)	384	ring 3 out of plane def. (s), NH2 ω (m), CH2 ω (w), N16-C15-C5 δ (m)
	414	ring 1,2 in plane def. (m), CH2 ρ (m), N16-C16-C5 τ (m)
	426	COO^- ρ (w), NH2 ρ (vs), CH ring 1 out of plane def. (vs)
438 (vw)	428	CH2 ρ (s), CH ring 1 out of plane def. (s), COO^- ρ (w)
	490	ring 1,2 in plane def. (s)

515 (vw)	513	CH2 τ (s), NH2 τ (s) COO^- ρ (w), C18-C17-C15 δ (m), CH ring 3 in plane def. (w), C15-H26 δ (s)
534 (vw)	518	ring 1,2,3 out of plane def. (m)
	570	ring 1,2 in plane def. (s), CH2 ρ (w), NH2 ω (w)
	583	ring 1,2,3, out of plane def. (s)
	619	CH2 ρ+ω (s), COO^- ω (m)
645 (vw)	649	ring 1,2,3 in plane def. (w), NH2 ω (m), COO^- ω (m), CH2 ρ (m)
657 (vw)	666	ring 3 out of plane def. (s)
	670	CH2 ρ (s), COO^- ω (w), C2-C6 out of plane def. (m)
	687	ring 1,2 in plane def. (s)
691 (vw)	699	ring 3 out of plane def. (s), NH2 ω (m), COO^- δ(w)
705 (vw)	705	CH ring 1 out of plane def. (s), ring 1,2 out of plane def. (w)
750 (vw)	736	CH ring 1 out of plane def. (s),
776 (w)	764	NH2 ω (vs), COO^- δ (m), C15-C17-C18 δ (m), CH2 ρ (m), ring 3 in plane def. (vw), C15-H26 δ (s)
	782	CH ring 3 out of plane def. (s)
	815	NH2 ω (w), ring 1,2,3 in plane def. (s)
835 (vw)	831	CH ring 1 out of plane def. (s)
	848	CH ring 3 out of plane def. (s), NH2 ω (vw)
869 (vw)	852	CH ring 3 out of plane def. (m), NH2 ω (s), CH2 ρ (s)
884 (vw)	884	ring 1,2,3 in plane def. (s) NH2 ω (m)
	901	NH2 ω (vs), COO^- δ (w), CH2 τ (s)
	909	CH ring 1 out of plane def. (s)
920 (vw)	914	COO-in plane bend. δ (m), NH2 ω (m), CH2 τ (m), C18-c17-C15 δ (s), CH ring 3 in plane def. (w)
	938	ring 2 in plane def. (m), NH2 τ (s), CH2 ω +ρ (m)
	948	CH ring 1 out of plane def. (s)
982 (vw)	971	O1-C5 ν (m), CH ring 3 in plane def. (m), NH2 τ (s), CH2 τ (s), C15-C17 ν (m)
	994	NH2 τ (m), ring 1,2 in plane def. (m), ring 3 in plane def. (s)
	1003	CH ring 3 in plane def. (s), CH ring 1 in plane def. (m),
1010 (m)	1007	CH ring 3 in plane def. (s), CH ring 1 in plane def. (m)
1027 (m)	1045	ring 1 in plane def. (s), C9-S10 ν (m), CH ring 3 in plane def. (m)
1060 (m)	1069	NH2 ω (s), CH2 τ (s), C5-C15-C17 ω (m)

1068 (m)	1107	CH ring 1 in plane def. (s)
	1109	CH2 τ (s), NH2 τ (s), C15-C26 δ (m)
	1144	CH ring 1 in plane def. (s)
	1170	CH ring 2 in plane def. (s), C15-H26 δ (m) NH2 τ (w), CH2 ω (w)
1182 (w)	1184	ring 3 in plane def. (s), CH2 ω (m)
1219 (w)	1211	CH ring 1 in plane def. (m), ring 2 in plane def. (m), C6-N7-C8 ν (s), ring 3 in plane def. C2-O1 ν (s), CH2 ω (m), .C15-H26 δ (m), NH2 τ (w)
1233 (w)	1235	CH ring 1 in plane def. (s), ring 2 in plane def. (w), CH ring 3 in plane def. (m), C2-O1 ν (w), CH2 ω (m), C15-H26 δ (m), NH2 τ (w)
1240 (w)	1242	CH ring 1 in plane def. (s), CH2 ω (s), C15-H26 δ (m), CH ring 3 in plane def. (m), NH2 τ (m)
1250 (vw)	1252	CH2 τ (s), C15-H26 δ (m), NH2 τ (m)
1273 (m)	1275	CH ring 1 in plane def. (s), N7-C8 ν (m), O1-C2 ν (m)
1284 (m)	1302	CH2 ω (s), C15-H26 δ (s), C2-C3-H24 δ (m)
1310 (vw)	1308	ring 1,2, in plane def. (vs), C15-H26 δ (w), CH2 ω (w)
	1345	C15-H26 δ (vs), CH2 ω (w), NH2 τ (s), C3-C4 ν (m)
1375 (w)	1365	CH ring 3 in plane def. (m), ring 3 in plane def. (m), C15-H26 δ (vs), NH2 τ (w)
1397 (w)	1382	C17-C18 ν (vs), CH2 ω (m), COO^- ν_{sym} (m), C15-H26 δ (w)
1414 (w)	1418	CH ring 1 in plane def. (s), C8-C9 ν (s),
	1434	CH2 δ (vs)
1445 (vw)	1437	CH ring 1 in plane def. (s), ring 1,2 in plane def. (m),
1473 (w)	1474	C6-N7 ν (vs) (C2-C3+C4-C5) ν (s), CH ring 1 in plane def. (w), C15-H26 δ (m),
1523 (vs)	1512	N7-C6-C2 ν_{asym} (s), C4-C5 ν (s), C15-H26 δ (m), CH ring 1 in plane def. (w)
	1537	COO^- ν_{asym} (vs), H27-C17-C18 δ (s)
	1542	ring 1 in plane def. (m), CH ring 1 in plane def. (m)
1578 (s)	1566	ring 1,2,3 in plane def. (m), CH ring 1,3 in plane def. (m), C15-H26 δ (w)
1595 (s)	1586	ring 1,2,3 in plane def. (s), CH ring 1,3 in plane def. (s)
1632 (s)	1629	NH2 δ (s)
2920 (vw)	2940	CH2 ν_{sym} (s)
	2971	C15-H26 ν (vs), CH2 ν_{asym} (w)
	2996	C15-H26 ν (m), CH2 ν_{asym} (s)
3064 (vw)	3063	CH ring 1 ν_{asym} (s)

	3074	CH ring 1 ν_{asym} (s)
	3084	CH ring 1 ν_{asym} (s)
	3091	CH ring 1 ν_{sym} (s)
	3136	CH ring 3 ν_{asym} (vs)
	3157	CH ring 3 ν_{sym} (s)
3380 (vw)	3338	NH2 ν_{sym} (vs)
3420 (vw)	3423	NH2 ν_{asym} (vs)

Abbreviations: w-weak; m-medium; s-strong; v-very; ring 1-phenyl ring; ring 2-thiazole ring; ring 3-furan ring; δ-bending: ρ-rocking; τ-twisting; ω- wagging; ν-stretching; sym-symmetric; asym-asymmetric; def-deformation.

In Fig. 3 experimental FT Raman spectrum of salt 1 is compared with theoretical Raman bands intensities. A good correspondence can be observed between these spectra.

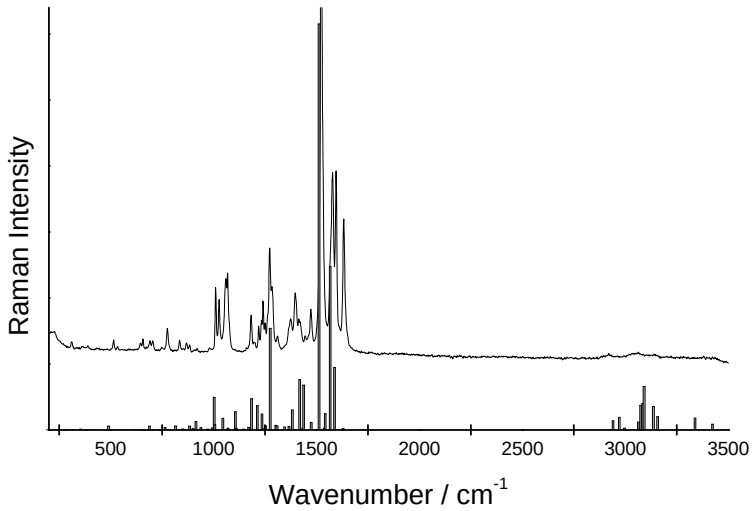

Fig. 3. FT-Raman spectrum of solid state of sodium salt of 3-amino-3-[(5-benzothiazole-2yl)-furan-2yl]-propanoic acid (a) and the calculated Raman intensities (B3LYP/6-31 G(d)) (b).

The observed disagreement between the theory and experiment could be a consequence of the anarmonicity and the general tendency of the quantum chemical methods to overestimate the force constants at the exact equilibrium geometry [15]

The most intense band at 1523 cm^{-1} can be assigned to N7C6C2 asymmetric stretching and C4C6 stretching vibrations, together with C15H26 bending vibration.

Symmetric stretching vibration of carboxylate group (COO^-) is present as medium intensity band at 1397 cm^{-1} together with C17C18 stretching and C17H27H28 wagging vibrations.

Ring 1. 2 and 3 (for rings number see abbreviation from Table 1) in plan deformation and CH ring 1 and 3 in plan deformation vibrations are present at 1578 and 1598 cm^{-1}. The bending and wagging vibrations of NH_2 group give the peaks at 1632 and 1060 cm^{-1}. The weak band at 776 cm^{-1} is assigned to NH_2 wagging and COO^- bending vibrations. NH_2 symmetric and asymmetric stretching vibrations appear as very weak bands in solid state FT Raman spectrum at 3380 and 3424 cm^{-1}.

B. Adsorption on silver surface

Salt 1 SER spectrum in silver sol is compared wit solid state Raman spectrum in Fig. 4. Table 2 presents SERS and Raman data.

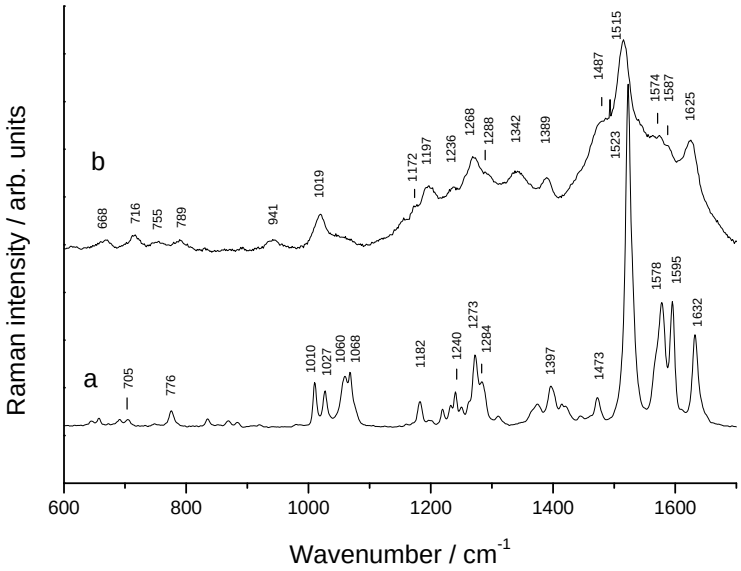

Fig. 4. FT-Raman solid sate (a) and SERS (b) (c=1.4 10^{-3} mol/L) spectra of sodium salt of 3-amino-3-[(5-benzothiazole-2yl)-furan-2yl]-propanoic acid.
Only spectral range of interest is presented.

Table 2.

SERS and Raman data (cm^{-1}) of salt 1 molecule.

FT Raman solid satae	SERS pH 8	Assignment
657(vw)	671(w)	ring 3 out of plane def.
705 (vw)	717 (w)	CH ring 1 out-of-plane def.
776 (w)	789 (w)	NH2 ω(vs), COO^- δ (m), C15-C17-C18 δ (m), CH2 ρ (m), C15-H26 δ (s)
1027 (m)	1019 (m)	ring 1 in plane def. (s), C9-S10 ν (m), CH ring 3 in plane def. (m)
1060 (w)	1046 (sh)	NH2 ω (s), CH2 τ (s), C5-C15-C17 ω (m)
1182 (w)	1179 (w)	ring 3 in plane def. (s), CH2 ω (m)
1240 (w)	1236 (w)	CH ring 1 in plane def. (s), CH2 ω (s), C15-H26 δ (m), NH2 τ (m)
1273 (m)	1268 (m-s)	CH ring 1 in plane def. (s), N7-C8 ν (m), O1-C2 ν (m)
1397 (m)	1389 (m)	C17-C18 ν (vs), CH2 ω (m), COO^- ν_{sym} (m), C15-H26 δ (w)
1473 (w-m)	1487 (sh)	C6-N7 ν (vs) (C2-C3+C4-C5) ν (s), CH ring 1 in plane def. (w), C15-H26 δ (m),
1523 (vs)	1515 (s)	N7-C6-C2 ν_{asym} (s), C4-C5 ν (s), C15-H26 δ (m), CH ring 1 in plane def. (w)
1578 (s)	1574 (sh)	ring 1,2,3 in plane def. (m), CH ring 1,3 in plane def. (m), C15-H26 δ (w)
1595 (s)		ring 1,2,3 in plane def. (s), CH ring 1,3 in plane def. (s)
1632 (s)	1625 (s-m)	NH2 δ (s)

Abbreviations : w-weak, m-medium, s-strong, v-very sh-shoulder, ring 1- phenyl ring, ring 2- thiazol ring, ring 3-furan ring.
ν-stretching, δ-bending, ω-wagging, τ-twisting, ρ-rocking,

The origin of the enhancement of Raman scattering cross section at rough surface has been an active field of research. The general consensus attributes the observed enhancement to contribution from two mechanisms: one electromagnetic enhancement and chemical effect [16, 17]. The electromagnetic mechanism of the Raman enhancement is based on the coupling of the radiation field with surface plasmons of the metal. In the chemical mechanism, based on a change in the molecular polarizability arising from the interaction with the metal substrate, an important role is played by the charge–transfer effect due to the resonant excitation into a charge-transfer transition of an adsorbate-metal complex [17, 18].

In the Fig. 4 the shift in the peak positions and the change in relative intensities of the SERS bands compared with normal Raman bands can is observed which indicate the interaction between the salt 1 molecule and silver surface and a chemisorption process on this surface.

The SERS band are broader than the corresponding Raman bands probably due to different adsorption sites on metallic surface.

The background signal around 1200-1600 cm^{-1} is due to the photo- or termal decomposition of the salt 1 specie which form carbon layer on the silver surface. [19]

The pH value of 8 was obtained in the sol after adding a small amount of the 10^{-2} aqueous solution of salt 1. At this pH value is expected to have the NH_2 and COO^- groups to be present in the structure of the adsorbed state.

Symmetric stretching vibration of carboxylate group is present in SER spectra at 1389 cm^{-1}. Its peak position is shifted to lower wavenumber by 8 cm^{-1} with respect to corresponding Raman band (1397 cm^{-1}).

According to literature [20] COO^- group can be bonded to silver surface via its π electron system when the corresponding peak position in adsorbed state is shifted to lower wavenumber by much as 6 cm^{-1} compared to the free molecule. The asymmetric stretching vibration of carboxylate group was barely discernable in the SER spectrum when adsorption occurred via π system [21]. On the other hand a blue shift of the symmetric COO^- stretching mode upon surface adsorption was observed in SER spectrum of benzoic acid on silver electrod surface via its oxygen lone pair electrons.

By inspection of Fig. 4 and Table 2 the red shift by 8 cm^{-1} of the symmetric COO^- stretching band is observed in SER spectrum of salt 1 molecular specie at pH 8 value in comparison with Raman spectrum, which confirm the binding of this group on the silver surface via π electron system of this group. The absence of asymmetric COO^- stretching vibration in SER spectrum reinforce the idea of the interaction of this group on silver surface via its π electron system.

The interaction between negatively charged COO^- group and silver surface is expected having in view the positive charge of silver surface.

According to the surface selection rules for Raman scattering [18, 23] the vibration of the adsorbed molecule, which has a polarizability tensor component normal to the surface will be preferentially enhanced. Stretching vibration are assumed to have large component of the polarizability along to bond axis.

The small intensity of the symmetric stetching band of carboxylate group observed in SER spectrum of salt 1 indicate the tilted close to flat orientation of this group with respect to the silver surface.

The presence of the weak COO^- in-plane bending vibration at 789 cm^{-1} reinforce the proposed orientation .

The bending vibration of NH_2 group is present in SER spectrum with medium intensity at 1625 cm^{-1}. The change in the peak position of this band compared to corresponding Raman band (1632 cm^{-1}) indicate the interaction of this group with metallic surface. NH_2 wagging vibration is present in Raman spectrum as medium intense band at 1060 cm^{-1} (Fig. 4a). In SER spectrum a weak and broad band is observed in this spectral region. Twisting vibration of the NH_2 group is also present in SER spectrum at 1236 cm^{-1}.

The presence in SER spectrum of the out-of-plane vibrational modes of NH_2 group and the very weak intensitie of stretching vibrations of this group, indicate the tilted to flat orientation of this group with respect to the silver surface.

In plane deformation modes of ring 1,2 and 3 (see abbreviations on the Table 2 for the rings number) located in SER spectrum at 1574 and 1587 cm^{-1} have very weak intensities as compared with corresponding Raman bands (1578 and 1595 cm^{-1}). Also N7C6C2 asymmetric stretching and C4C5 stretching vibrations located at 1515 cm^{-1} appear in SER spectrum with weaker intensity compared to the normal Raman spectrum (1523 cm^{-1}).

According to surface selection rules we suppose a weak interaction of the rings with metallic surface and tilted to flat orientation of these rings with respect to silver surface. This rings orientation is very probable taking in account the molecular structure presented in Fig.2 in which rings plane coincide with the COO^- plane, last group being oriented near to flat position on the silver surface. The presence in SER spectrum of ring 1, 2 and 3 in-plane deformation vibration at 1019, 1236, and 1268 cm^{-1} reinforces the proposed orientation of this plane with respect to silver surface. The interaction between the rings and metalic surface via their π electron system is posible having in view the shift to lower wavenumber by approximatlly 10 cm^{-1} of the peak positions specific to rings vibrations and their bandwidths substantialy increased in adsorbed state [24].

Conclusions

DFT calculation of sodium salt of 3-amino-3-[(5-benzothiazole-2yl)-furan-2yl]-propanoic acid have been performed at the B3LYP/6-31G(d) level of theory. The assignment of the vibrational modes was accomplishes and a good agreement was obtained between the theoretical vibrational wavenumbers and the experimental FT Rama data. Good SER spectrum was obtained in weak alkaline environments indicating a chemisorption of salt 1 molecule on silver surface. Salt 1 molecule was bonded to the silver surface through π electron system of carboxylate group which has tilted close to flat orientation on the surface. Phenyl, thiazol and furan rings plane have also close to flat orientation to the metallic surface.

REFERENCES

1. F. Fulop, *Chem*. Rev.**101**, 2181 (2001)
2. K. Gademann, T. Hintermann, J. V. Screiber, *Current. Med. Chem*., **6**, 905, (1999)
3. W. T. Lippincott, A. B. Garett, F. H. Verhoek, *"Chemistry. A study of matter"* Ed. J. Wiley an Sons 1977
4. G. Dryhusrst, *"Electrochistry of Biological Molecules*"New York, 1977 p. 493.

5. V. M. Rodionov, E. F. Malivinskaya, *Ber.* **59,** 2952, (1926)
6. T. K. Lee, D. M. Meisel, *J. Phys. Chem***. 87**, 3391, (1982)
7. Gaussian 98, Revision A 7, M. J. Frisch, G. W. Trucks, H. B. Schlegel, G. E. Scuseria, M. A. Robb, J. C. Burant, S. Dapprich, J. M. Millam, A. D. Daniels, K. N. Kudin, M. C. Strain, O. Farcas, J. Tomasi, V. Barone, M. Cossi, R. Cammi, B.Mencucci, C. Pomelli, C. Adamo, S. Clifford, J. Ochterski, G. A. Petersson, P. Y. Ayala, Q. Cui, K. Morokuma, D, K. Malick, A. D. Rabuck, K. Raghavachari, J. B. Foresman, J. Cioslowski, J. V. Ortiz, A. G. Baboul, B. B. Stefanov, G. Liu, A. Liashenko, P. Piskorz, I. Komaromi, R. Gomperts, R. L. Martin, D. J. Fox, T. Keith, M. A. Al-laham, C. Y. Peng, A. Nanayakkara, C. Gonzales, M. C. Challacombe, P. M. Gill, B. Johnson, W. Chen, M.W. Wong, J. L. Andes, C.Gonzales, M. Head-Gordon, E. S. Replogle, J. A. Pople, Gaussian Inc. Pittsburgh P. A. (1998).
8. J. J. P. Stewart, *J. Comp. Chem***. 10**, 209, 221, (1989)
9. M. J. S. Dewar, C. H. Reynolds, *J. Comp. Chem***. 2**, 140, (1986)
10. A. D. Becke, *J. Chem. Phys.,* **98**, 5648, (1993)
11. C. Lee, W. Yang, R. G. Parr, *Phys Rev*. **B 37**, 785 (1988)
12. W. J. Hehre, L. Radom, P. V. R. Schleyer, J. A. Pople, *"Ab initio Molecular Orbital Theory"* J. Wiley and Sons, N. York, 1986.
13. A. P. Scott, L. Radom, *J. Phys. Chem*., **100**, 16502, (1996)
14. a) MOLEKEL 4.2 P. Flukiger, H. P. Luthi, S. Portmann, J. Webwe, Swiss. Center for Scientific Computing, Manno (Switzerland) 200-2002. (b) S. Portmann, H. P. Luthi, MOLEKEL; *"An InterativeMolecular Graphyc Tool" Chemia*, **54**, 766, (2000)
15. G. Rouhut, P Pulay *J. Phys. Chem*. **99**, 3093, (1995).
16. M. Moskovits, *Rev. Mod. Phys***., 57**, 783, (1985)
17. T. Vo-Dinh, *Trends in Analyt. Chem*., **17**, 557, (1998)
18. J. A. Creighton, Surf. Sci., 124, 208, (1983).
19. T. Iliescu, M. Vlassa, M. Caragiu, I. Marian, S. Astilean, *Vibr. Spectrosc*. **8**, 451, (1995)
20. Y. J. Kwon S. B. Lee, K. Kim, M. S. Kim, *J. Mol. Struct*. **318**, 25, (1994).
21. H. Park, S. B. Lee, K. Kim, M. S. Kim, *J. Phys. Chem*. **94**, 7576, (1990)
22. Y. J. Kwon, D. H. Soon, S. J Ahn, S. Kim, K. Kim, *J Phys. Chem*. **98**, 8481, (1994).
23. M. Moskovits, D. P. Dillella, *J. Chem. Phys*. **73**, 6068 (1980)
24. S. T. Oh, K. Kim, M. S. Kim, *J Phys. Chem*., **95**, 8844, (1991)

STUDIA UNIVERSITATIS BABEŞ BOLYAI, PHYSICA, L, 1, 2005

CONTRIBUTIONS TO THE ULTRASONIC STUDY OF MOLECULAR INTERACTIONS IN THE DICHLOROMETHANE – BENZENE MIXTURES

A. CIUPE*, I. LENRT*

**Faculty of Physics, "Babeş-Bolyai" University, Cluj-Napoca, Romania*

ABSTRACT. Ultrasonic propagation velocity, density, dynamic viscosity coefficient and thermal expansion coefficient measurements were carried out un the binary liquid system dichloromethane – benzene for the pure components and for different dichloromethane concentrations at different temperatures in the range 283 – 303 K. Based on the experimental data quantities as: the adiabatic compressibility coefficient, the available volume, the a_y force parameter, the free volume were calculated. A comparison between different internal pressure formulas, in connection with the ultrasonic propagation velocity as a common parameter is made. The obtained results give information about the contribution of different types of interactions to the overall effect of molecular interaction in the studied system and about their dependence on the dichloromethane concentration and the temperature of the mixture.

INTRODUCTION

The propagation of ultrasound in the matter is characterised by the propagation velocity and the absorption coefficient. The wave energy transfer to the medium is determined by the individual properties (structure, size, shape, polarity, etc.) of the molecules and the intermolecular forces acting between them. In this respect the ultrasonic propagation velocity can offer qualitative information about the molecular interaction in pure liquids and liquid mixtures [1 ÷ 5].

The dispersion forces are operative in all the systems. The mechanisms that lead to stronger interaction are dipole – dipole interaction, dipole – induced dipole interaction, hydrogen bonding, charge transfer interaction, etc. [5,6,7].

The paper deals with the results obtained in the ultrasonic study of the dichloromethane – benzene system on the basis of ultrasound propagation velocity, density, viscosity coefficient and thermal expansion coefficient measurements over the whole concentration range at different temperatures in the interval 286 – 303 K.

Theory

On the basis of the experimental data the following quantities were calculated:

- the mean molar volume: $\overline{V} = \overline{M}/\rho$, (1)

where $\overline{M}$ is the molar mass;

- the adiabatic compressibility coefficient, defined as:

$$\beta_S = -\frac{1}{V_0}\left(\frac{\partial V}{\partial p}\right)_S \tag{2}$$

calculated with the formula: $\beta_S = \frac{1}{\rho c^2}$; (2')

- the a_y parameter as a measure of the intensity of intermolecular forces in the mixture, which is related to the constant "a" in the van der Waals state equations by means of the following equation of definition [3]:

$$a_y = \frac{\gamma a}{\overline{M}^2} \tag{3}$$

where $\gamma = C_P / C_V$ the ration of molar heats at constant pressure, respectively at constant volume; this parameter was calculated by the formula:

$$a_y = \frac{c^2}{2\rho}; \tag{3'}$$

- the available volume V_d, defined as:

$$V_d = \overline{V} - b, \tag{4}$$

calculated by the relation [2]:

$$V_d = \overline{V}\left(1 - c / c_\infty\right), \tag{4'}$$

where b is the covolume and c_∞ =1600 m/s is a limiting ultrasonic velocity for homologue series of organic liquids for the case $M \to \infty$;

- the free volume V_f defined as the volume of the allowed moving space for the molecule center in one mole, defined as [2]:

$$V_f = V\left(1 - \sqrt[3]{B / V}\right)^3 \tag{5}$$

was calculated by means of the formula [8]:

$$V_f = k\left(\overline{M}c / \eta\right)^{3/2} \tag{5'}$$

where $k = 3{,}57 \cdot 10^{-15}$.

The internal pressure has different expressions owing either to the use of various models or to the introduction of some approximations. That is reflected by the discrepancy of the obtained values [5, 9].

The internal pressure defined by:

$$p_i = \left(\frac{\partial U}{\partial V}\right)_T \tag{6}$$

(U being the internal potential energy) results from the contribution of all attractive and repulsive potentials [10], can be expressed as:

$$p_i = T\left(\frac{\partial p}{\partial T}\right)_V - p \qquad (6')$$

where p is the external pressure, which usually can be neglected in the case of liquids.

Based on the thermodynamic arguments, neglecting the external pressure and after performing some changes [10] the following formulas are obtained in order to calculate the internal pressure with experimental data:

$$p_i = \frac{\alpha T}{\beta_T} = \frac{\alpha T}{\gamma \beta_S} = \frac{\alpha}{\gamma} T \rho c_S^2 \qquad (7)$$

respectively:

$$p_i = \frac{\alpha T \rho c_S^2 C_P}{C_P + T\alpha^2 M c_S^2} \qquad (8)$$

where α is the volume expansion coefficient at constant pressure, T is the absolute temperature, ρ is the density, c_S is the adiabatic ultrasound propagation velocity, β_T and β_S is the thermal and the adiabatic compressibility coefficients.

The van der Waals internal pressure was obtained on the basis of a simplified model in which the intermolecular interactions are limited to that of attraction by means of dispersion forces. Thus expressing the potential component of the internal energy U corresponding to all pairs from a number N of molecules by:

$$U = -\frac{2}{3}\pi N^2 \frac{a}{r_0^3}\frac{1}{V} = -\frac{a}{V}$$

from (6) the van der Waals' internal pressure formula is obtained:

$$p_{iW} = \frac{a}{V^2}, \qquad (9)$$

where "a" is a constant and V is the molar volume.

With a view to get the relation between the real internal pressure p_i, deduced by thermodynamic reasons and the van der Waals' internal pressure p_{iW} it is necessary to express p_{iW} as a function of the ultrasound propagation velocity c_S that is defined by:

$$c_S = \gamma\left(\frac{\partial p}{\partial \rho}\right)_T. \qquad (10)$$

By making some approximations [3], from (9) and (10) it results:

$$p_{iW} = \frac{\rho c_S^2}{2\gamma} \qquad (11)$$

and from (7) and (11) we got [10] the relation we sought for:

$$p_i = 2\alpha T p_{iW} \quad (12)$$

where $2\alpha T$ represents the correction coefficient of the van der Waals' internal pressure.

Another relation proposed [11] for the estimate of internal pressure, based on the cellular model for liquids, relates it to the free volume as follows:

$$p_{ic} = \frac{b_1 RT}{V_f^{1/3} V^{2/3}} - p \quad (13)$$

where b_1 is a parameter depending on the degree of packing of the liquid molecules (can be taken as $b_1 = 2$ for cubic arrangement) and p is the external pressure.

The formula: $c = c_\infty \cdot s \cdot r$ (14)

found by Schaaffs [2] relates the propagation velocity c to the molecular structure of the liquid. Here s is the so called collision factor, describing the energy lost during the wave propagation and r is the degree of space filing. In relation (14):

$$r = \frac{B}{V} \quad (15) \quad \text{and} \quad s = \frac{b}{B} \quad (16)$$

where $B = \frac{4\pi}{3} R^3 N_A$ (R is the molecule radius and N_A is the Avogadro's number). R can be calculated by the formula:

$$R = \left[\frac{3}{4\pi N_A} \left(1{,}1 \frac{n_D^2 - 1}{n_D^2 + 2} \frac{M}{\rho} \right) \right]^{1/3} \quad (17)$$

where n_D is the standard refractive index..

The covolume b was calculated (for the pure components) from $\overline{V}$ and V_d by formulas (4) and (4').

The interstitial volume: $V_i = V\text{-}B$ (18)

Allows to estimate the relative interspace V_i/V and the space occupancy ratio B/V_i.

EXPERIMENTAL

In order to measure the ultrasonic velocity the method of optical diffraction by ultrasonic beams of 4MHz frequency was used with an accuracy of ± 0,2 % [12]. The density was measured by means of a picnometer with an accuracy of ± 0,2%. The dynamic viscosity coefficient measurements were carried out with the capillary viscosimeter. The thermal expansion coefficients were measured by means of a dilatometer. The measurements were carried out in temperature controlled conditions (± 0,1 K) within the range from 286 to 303 K. The refractive indexes were measured with an Abbe refractometer.

RESULTS AND DISSCUTIONS

The results for the pure components at 293 K are summarized in Table 1.

Table 1.

Some physical parameters of the pure components at 293 K

Para-meter	Measure unity	Benzene	Dichloro-methane	Parameter	Measure unity	Ben-zene	Dichloro-methane
M		78,11	84,93	V_d/V		0,164	0,314
ρ	Kg/m^3	878	1314	$V_f \cdot 10^3$	$m^3/kmol$	2,67	2,32
μ	D	0	1,56	$R \cdot 10^{10}$	m	2,26	1,97
c	m/s	1338	1097	$B \cdot 10^3$	$m^3/kmol$	29,1	19,2
n_D		1,5063	1,4242	s = b/B		2,5	2,28
$\eta \cdot 10^3$	Ns/m^2	0,65	0,81	r = B/V		0,328	0,300
$V \cdot 10^3$	$m^3/kmol$	88,85	63,95	$b \cdot 10^3$	$m^3/kmol$	74,31	43,85
$\beta \cdot 10^{10}$	m^2/N	6,353	6,325	$V_i \cdot 10^3$	$m^3/kmol$	59,75	44,75
a_y	m^5/kgs^2	1018	457	B/V_i		0,48	0,42
$V_d \cdot 10^3$	$m^3/kmol$	14,54	20,10	V_i/V		0,67	0,70

The studied system contains compound with different specific features. The non-polar molecules of benzene (C_6H_6) between which high intensity dispersion forces are acting as shown by the higher value of a_y, make a more compact structure, as indicate the values of r respectively B/V_i and the lower values of V_d/M respectively V_i/V. Their symmetric cyclic configuration approaches better to the spherical shape required by the model used, than the asymmetric configuration of the dichloromethane molecules (CH_2Cl_2). On the other hand dichloromethane is a polar liquid (μ = 1,56 D). Between its molecules orientation effects by dipole – dipole interactions as well as van der Waals dispersion forces occur. The mentioned features influence the values of the free volume (as a measure of the moving possibility of the molecule centers) and of the viscosity coefficient. Hence, the high value of V_f respectively the low value of η in the case of benzene reflect the freedom of rotation of its molecules. The small value of the free volume V_f and the high value of the viscosity in dichloromethane can be assigned to the effect of the rotation restriction of dichloromethane molecules caused by their non-spherical shape and by the orientation effect of the dipole – dipole interaction of the molecules.

The measured values of density propagation velocity, dynamic viscosity coefficient and thermal expansion coefficient obtained for the studied mixtures at different concentrations (χ_{CH2Cl2} is the mole fraction of dichloromethane) and different temperatures are presented in Table 2.

Based on the measured values using the above presented relations the adiabatic compressibility β_S, the a_y force parameter, the mean molar volume $\overline{V}$, the available volume V_d, the free volume V_f were calculated. These results are presented in Table 3a.

Also the van der Waals' internal pressure p_{iW}, the thermodynamic internal pressure p_i, the $2\alpha T$ coefficient and the internal pressure based on the cellular model p_{ic} were calculated. The obtained values are included in Table 3b.

To illustrate the obtained results in a graphical plotting following isotherms were selected: the a_y force parameter (Fig. 1), the van der Waals' internal pressure p_{iW} (Fig. 2), the thermodynamic internal pressure p_i (Fig. 3) and the internal pressure based on the cellular model p_{ic} (Fig. 4) as a function of the mole fraction of the dichloromethane.

Table 2.

Measured values for some physical parameters in dichloromethane – benzene mixture

Concentration χ CH_2Cl_2	T [K]	ρ [kg/m^3]	c [m/s]	$\eta \cdot 10^3$ [Ns/m^2]	α [K^{-1}]
1	2	3	4	5	6
0,0	286	886,2	1387	0,72	
	288	884,2	1372		113,2
	293	879,2	1338	0,65	113,9
	298	874,2	1307		114,5
	303	869,2	1287	0,56	115,2
0,06	286	904,1	1343	0,68	
	288	903,3	1338		114,7
	293	898,9	1317	0,64	115,5
	298	892,8	1288		116,1
	303	886,6	1260	0,56	116,8
0,25	286	971,8	1289	0,68	
	288	974,5	1281		119,1
	293	964,3	1260	0,66	119,8
	298	957,3	1240		120,5
	303	953,1	1220	0,60	121,3
0,47	286	1049,1	1230	0,71	
	288	1047,4	1224		124,1
	293	1043,2	1207	0,69	125,0
	298	1038,5	1185		125,8
	303	1031,8	1163	0,61	126,6
0,67	286	1137,8	1184	0,74	
	288	1138,7	1175		128,6
	293	1137,7	1156	0,72	129,5
	298	1132,7	1139		130,4
	303	1123,9	1121	0,65	131,3
0,84	286	1243,6	1149	0,79	
	288	1228,0	1139		132,5
	293	1220,3	1116	0,75	133,5
	298	1214,2	1097		134,5
	303	1210,7	1080	0,69	135,4

1,0	286	1337,3	1118	0,82	
	288	1327,5	1112		136,1
	293	1314,5	1097	0,81	137,1
	298	1305,4	1079		138,1
	303	1299,3	1058	0,73	139,1

Table 3 a

Concentration χ CH_2Cl_2	T [K]	$\beta \cdot 10^{10}$ [m^2/N]	a_y [m^5/kgs^2]	$\overline{V} \cdot 10^3$ [$m^3/kmol$]	$V_d \cdot 10^3$ [$m^3/kmol$]	$V_f \cdot 10^3$ [$m^3/kmol$]
1	2	3	4	5	6	7
0,0	286	5,867	1085	88,15		0,230
	288	6,008	1064	88,35	12,59	
	293	6,353	1018	88,85	14,54	0,235
	298	6,696	977	89,36	16,36	
	303	6,946	953	89,87	17,58	0,272
0,06	286	6,133	997	86,91		0,218
	288	6,186	990	86,99	14,24	
	293	6,414	965	87,41	15,46	0,232
	298	6,752	929	88,01	17,16	
	303	7,104	895	88,63	18,83	0,265
0,25	286	6,193	855	82,16		0,210
	288	6,253	841	81,93	16,33	
	293	6,532	823	82,80	17,59	0,212
	298	6,793	803	83,41	18,76	
	303	7,049	781	83,77	19,89	0,233
0,47	286	6,300	721	77,48		0,188
	288	6,373	715	77,67	18,24	
	293	6,580	698	77,92	19,14	0,190
	298	6,857	676	78,27	20,30	
	303	7,165	655	78,78	21,52	0,217
0,67	286	6,269	616	72,69		0,172
	288	6,361	606	72,63	19,29	
	293	6,577	587	72,69	20,17	0,170
	298	6,805	573	73,02	21,04	
	303	7,080	559	73,59	22,03	0,192
0,84	286	6,091	531	67,45		0,150
	288	6,277	528	68,30	19,68	
	293	6,579	510	68,73	20,79	0,157
	298	6,843	495	69,69	21,90	
	303	7,081	482	69,28	22,52	0,169
1,0	286	5,982	467	63,51		0,139
	288	6,092	466	63,98	19,51	
	293	6,325	458	63,95	20,10	0,141
	298	6,580	446	65,06	21,18	
	303	6,875	431	65,37	22,14	0,154

Table 3 b

Concentration $\chi_{CH_2Cl_2}$	T [K]	$P_{iw} \cdot 10^{-8}$ [N/m^2]	$P_i \cdot 10^{-8}$ [N/m^2]	$2\alpha T$	$P_{ic} \cdot 10^{-8}$ [N/m^2]
1	2	3	4	5	6
0,0	288	5,745	3,746	0,652	
	293	5,595	3,732	0,667	3,970
	298	5,373	3,664	0,682	
	303	5,140	3,588	0,698	3,860
0,06	288	5,680	3,752	0,660	
	293	5,523	3,734	0,676	4,020
	298	5,311	3,670	0,691	
	303	5,089	3,599	0,707	3,930
0,25	288	5,539	3,799	0,686	
	293	5,343	3,750	0,702	4,280
	298	5,174	3,715	0,718	
	303	5,016	3,687	0,753	4,260
0,47	288	5,341	3,813	0,714	
	293	5,193	3,801	0,732	4,620
	298	5,018	3,759	0,749	
	303	4,839	3,711	0,767	4,540
0,67	288	5,259	3,892	0,740	
	293	5,113	3,875	0,758	5,030
	298	4,957	3,851	0,777	
	303	4,791	3,009	0,795	4,950
0,84	288	5,232	3,992	0,763	
	293	5,034	3,937	0,782	5,360
	298	4,851	3,885	0,801	
	303	4,708	3,861	0,820	5,370
1,0	288	5,287	4,139	0,783	
	293	5,085	4,083	0,803	5,850
	298	4,865	4,039	0,823	
	303	4,730	3,983	0,842	5,770

The a_y force parameter derived on the basis of the van der Waals model, as a measure of only the attractive interactions by dispersion forces, has a high value in benzene. With the increase of the dichloromethane concentration (Fig. 1), the a_y value decreases toward the value corresponding to pure dichloromethane, a lower value in agreement with the decrease of carbon atoms number in the molecule from 6 in benzene to 1 in dichloromethane

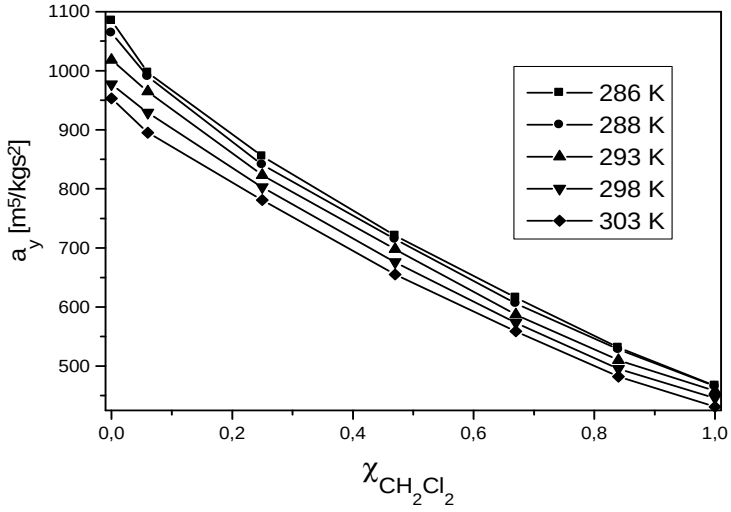
1100
1000
900
800
700
600
500
a_y [m⁵/kgs²]
286 K
288 K
293 K
298 K
303 K
0,0
0,2
0,4
0,6
0,8
1,0
χ CH2Cl2

Fig. 1.

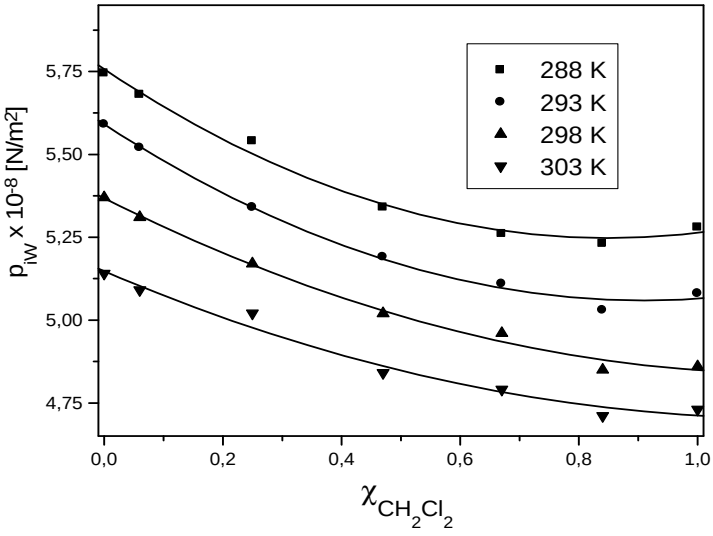
5,75
5,50
5,25
5,00
4,75
p_iw x 10⁻⁸ [N/m²]
288 K
293 K
298 K
303 K
0,0
0,2
0,4
0,6
0,8
1,0
χ CH2Cl2

Fig. 2.

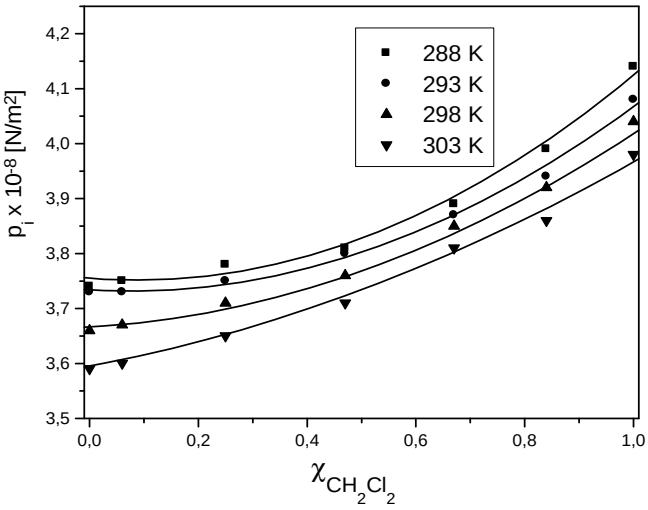

Fig. 3.

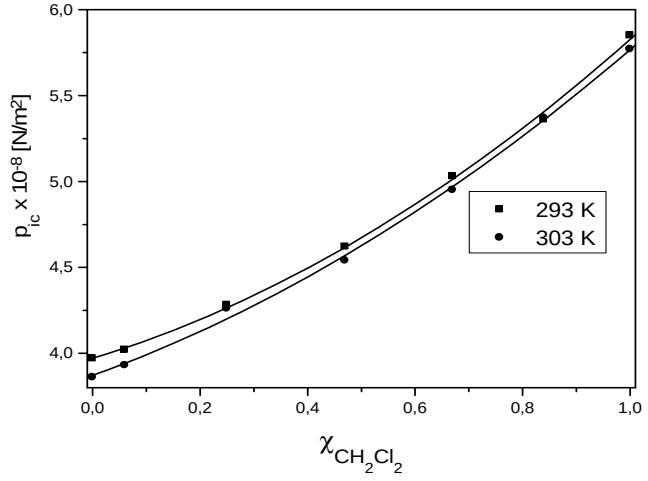

Fig. 4.

Van der Waals' internal pressure definition is based on a simplified model restrictive in character, consequently, the values obtained are characterized by the deviations from the real ones especially in the case of liquids. The magnitude of the deviation corresponds to intermolecular interactions, omitted from the van der Waals' model, which are limited to those of dispersion for some simplified molecules from the point of view of their shape and their interaction number.

The van der Waals' internal pressure has a higher value in benzene (Fig. 2), decreases with increasing mole fraction of dichloromethane and after passing a minimum riches the value corresponding to the pure dichloromethane, a lower one as in benzene in agreement with the evolution of the dispersion forces described by the a_y parameter.

The correction factors $2\alpha T$ having values less than one (Table 3b) lead to values of the internal pressure p_i (derived on thermodynamic basis) lower than those of p_{iW}. The lowering of the difference between p_i and p_{iW} with increasing temperature imposed by the correction factor reflects the prevalent role of rejection forces within the correction. The increase of temperature affects especially these interactions, which are overlooked by the van der Waals' model.

The van der Waals' pressure p_{iW} decreases with the increasing temperature (Fig. 2) in agreement to the a_y temperature dependence (Fig. 1). The temperature dependence of internal pressures p_i (Fig. 3) and p_{ic} (fig. 4) are similar to that of p_{iW} (Fig. 2).

Unlike p_{iW}, the internal pressure p_i, respectively p_{ic} increase with the concentration of dichloromethane (Fig. 3 and Fig. 4).

The correction factors $2\alpha T$ includes beside the contribution of the rejection forces to the internal pressure p_i (by the already mentioned decrease imposed to p_{iW}) the contribution of other attractive forces overlooked in the van der Waals' model, such as that of orientation and that of induction. In this respect, the increase of the correction factors $2\alpha T$ at a given temperature (Table 3b) respectively the increase of p_i with the increasing dichloromethane concentration can by assigned to the increase of attractive forces as a result of the gradual substitution of dispersion interactions acting in benzene by dipole – induced dipole induction forces between unlike molecules in the mixtures, respectively by dipole – dipole orientation forces between identical molecules of dichloromethane.

The high value of p_{ic} compared to that of p_i in dichloromethane results from the lower propagation velocity value respectively from the higher viscosity coefficient value in this component.

In agreement with the molecular mechanism of ultrasound propagation, the more compact structure, quantitatively described by the degree of space occupation r, ($r_{C6H6} \rangle r_{CH2Cl2}$) as well as the more efficient energy transmission, described by the collision factor s ($s_{C6H6} \rangle s_{CH2Cl2}$) in benzene, explain the higher value of propagation velocity in this component.

Between the polar molecules of dichloromethane orientation forces are acting in addition to that of dispersion ones (active in benzene too), what together with the deviation of the shape of this molecules from the spherical one explain the higher value of internal friction forces (η) in this case.

The mentioned results indicate that the cellular model on which the evaluation of p_{ic} is based, assign a grater importance to the contribution of the specific features: r, s, μ and molecular shape to the internal pressure value.

As a conclusion one can say that regarding the potential energy of intermolecular interactions (6) using the connection existing between p_i and p_{iW} it is possible to separate the contribution of the attraction forces from that of the rejection ones to the global potential energy.

REFERENCES

1. Lagemann R. T., Corey J. E., J. Chem. Phys., vol. 10, p. 759, 1942
2. Schaaffs W., Molekularakustik, Berlin, 1963
3. Melkonean L.G., Scorost' ultrazvuca I mejmolecularnoe pritiajenie v binarnih jidkih smesiah obrazuiuscih himicescoe soedinenie, in the volume Primenenie Ultrazvuk k Issledovanie Vescestvo, red. V.F. Nozdrev, B.B. Kudreavtev, Mopi, Moskva, 1956
4. Mishra R.L., Some Acoustical and Thermodynamic Parameters, D. Phys. Thesis, Allahabad Univ., India, 1977.
5. Jha D. K., Jha B. L., Acustica (Stutgart)75, p. 279-282, 1992
6. Venkatesu P. Prabhakara Rao M.V., J. Chem Eng. Data, 41 (4), p. 1056, 1996
7. Oswal S. L., Patel N. B., J. Chem Eng. Data, 40 (3), p. 845, 1995
8. Kupussami J., Suryanarayana C.V., J. Acoust, Soc. Indian, 4, p.75, 1976
9. Lenart I., Ciupe A., Auslander D., Academia Romana, Comisia de Acustica, Caiet 24, Bucuresti, p. 147 – 150, 1994
10. Ausländer D., Lenard I., Ciupe A., Contributions to the Ultrasonic Study of the Internal Pressure of Liquids, Acustica (Stuttgart), 81, p.75, 1995
11. Suryanarayana C.V., Indian L. Chem., 10, p. 713, 1972
12. H. Ţintea, L. Oniţiu, D. Ausländer, Studia Univ. "Babeş-Bolyai", series Mat.- Phys., 1, p.135, 1969
13. Lenart I., Ciupe A., Studia Univ. "Babes-Bolyai, Physica, XLVIII, 2, p. 49, 2003
14. Ciupe A., Lenart I., Studia Univ. "Babes-Bolyai, Physica, XLVII, 2, p. 41, 2002

STUDIA UNIVERSITATIS BABEŞ BOLYAI, PHYSICA, L, 1, 2005

LANGMUIR-PROBE STUDY OF THE HOT ELECTRON CYCLOTRON RESONANCE ION SOURCE PLASMA

L. KENÉZ[1], J. KARÁCSONY[1], A. DERZSI[1]

ABSTRACT. The electron cyclotron resonance (ECR) ion sources are high performance machines, which provide high intensity, highly charged ion beams. The most important part of these machines is the complex structure ECR plasma that is still not known properly. Local plasma diagnostic research was started in the ATOMKI-ECRIS laboratory. As a first step, the cold plasma regions have been studied. We showed that Langmuir-probes could be successfully used in certain conditions to get information on the cold plasma [1,2]. From the high performance point of view of the source much more important are the hot regions of the plasma. This paper deals with the exploration of these regions. Though energetic electrons are present in the ECR zone, we could measure probe characteristics without damaging the probe, at stabile operation conditions of the source. New shape of the voltage-current curves were observed, qualitative explanation of the curve shape was established assuming secondary electron emission of the probe. By computational study of the theoretical model the role of the secondary electron emission of the probe has been proved.

INTRODUCTION

The most important part of the Electron Cyclotron Resonance (ECR) Ion Sources (ECRISs) which determines their high performance operation is the ECR plasma. This has complex nature. The electron component contains cold and hot electron population. The hot electron component is located in the core of the plasma region. The position of the hot electron component is well determined by the magnetic configuration and the frequency of the microwave. These two determine the resonant zone where electron are stochastically heated and confined. The ion component of the plasma is also complex. Generally it contains multiply charged ions of different atomic species. Till now we concentrated on the cold plasma regions. It was determined axial, azimuth and radial electron density distributions and established a new theoretical model for evaluation of the characteristics, which takes into account the complex nature of the ion component of the plasma [1,2]. The present paper is devoted to the first results of the hot plasma experiments. The experiments were performed at the 14.5 GHz ATOMKI-ECR ion source [3].

[1] *Babeş-Bolyai University, Cluj-Napoca, RO-430000, Str. M. Kogălniceanu, Nr. 1, Romania*

Hot plasma experiments

The hot ECR plasma experiments must be carefully done. Beside the different kinds of difficulties described at the cold plasma experiments [1], additional problem is the presence of these energetic electrons trapped in the ECR zone. Due to the ECR effect the perpendicular energy of the electrons are some magnitudes higher than the parallel ones. Taking into account that the probe isn't cooled, this is a real danger source to the probe and insulation of the probe. To avoid probe damage during the experiments, we placed the probe in many distinct points and we concluded that a probe without cooling could be reliably used in such manner that only the tip of the probe enters the resonant zone. The insulated parts must remain outside the resonant zone otherwise the insulation can easily melt. Such places are the convex regions of the zone that can be reached with an off-axis introduced probe.

Of course, also in these cases, maximum attention must be paid to all ion source parameters to be certain that the probe and source are working properly during the experiments.

Many characteristics series were taken moving the probe by small steps toward the resonant zone, than pulling it backwards. The exact position of the resonant zone can be easily determined experimentally by pushing toward the resonant zone the sufficiently high negatively biased probe and monitoring the probe current in the mean time. When the probe reaches the resonant zone, a sudden increase of the probe current can be observed. For the experiments we generated oxygen plasma and tuned the source for O^{3+} production. The results were quite surprising: we obtained voltage-current (*U-I*) characteristics never encountered in the literature before. Such characteristics series are presented in Fig. 1.

It can be observed that far from the resonant zone, the well-known shaped cold plasma *U-I* curves were measured (*d = 9, 4, 3 mm* from the resonant zone). At *d = 2* mm distance from the ECR zone a slight minimum appears in the ion current region, which is emphasized as the probe approaches more-and-more the resonant zone. The position of the minimum also changes, it shifts toward higher negative voltages. The measured probe current at the minimum point is unusually high compared to the values measured in the cold plasma region (up to *9 mA* !!!). During the experiments the plasma was stabile; changes of the extracted ion currents were lower than 3%. As a first control measure we measured the *U-I* characteristics (curves) in the same points pulling the probe backwards, and obtained the same results. Though the temperature of the probe was high (during the experiments intense light was coming out of the plasma chamber), the probe did not damage. Later the visual check of the probe supported this assumption.

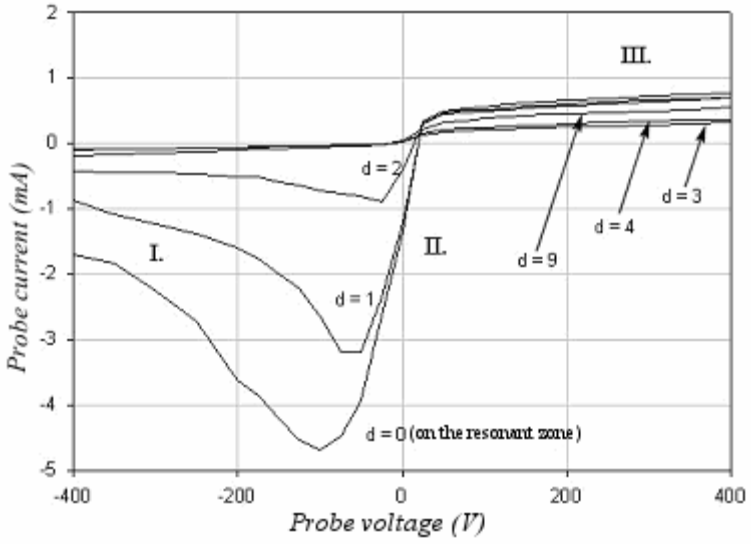

Fig. 1. Hot ECR plasma voltage-current characteristics series;
d - Distance between the probe and the resonance zone

To explain the above-presented characteristics we will take into account the role of secondary electron emission. Secondary electrons can result from either electron or ion bombardment. Ion secondary electron emission can be potential emission and kinetic emission. Because secondary electron emission coefficients σ can be greater than 1 for ion energies greater than 1 keV and potential emission is not depends on the ion energies, we will concentrate on the electron secondary electron emission. Secondary electron emission coefficients can be greater than 1 for incident electron energies of several hundred eV, thus in secondary electron emission the hot electron component of the ECR plasma will have a key role.

The shape of the curve can be interpreted by using the following qualitative model. In the electron current saturation region the probe attracts all primary electrons and repels all ions. Electrons on the resonant zone gain high perpendicular energies (ECR effect), while the parallel energies remain unchanged. When such hot electron collides with the probe surface it gives birth to a great amount of secondary electrons and also transfers energy to the probe that increases its temperature.

The secondary electrons are thermal ones, have low energies so they cannot leave the positive potential barrier of the probe and do not contribute to the total probe current. The electron current presents good saturation *(III)*. Decreasing the probe potential, but keeping it positive with respect to the local plasma potential, it collects some higher energy ions and higher energy secondary electrons can already leave the probe. Electron emission current appears as an

apparent ion collection current and so the total current will show a slowly decrease. If now the probe potential is made negative to the plasma potential, ions are collected in higher number, primary electrons compete with the repelling potential but still have sufficient energies to get collected and give birth to secondary electrons. These electrons are repelled from the probe surface. Because there is a great amount of secondary electrons, the total current falls rapidly *(II)* reaching a minimum value. The probe works as o self-emissive probe.

If we continue to decrease the probe potential the total probe current will increase. We can explain this behavior taking into account that the primary electrons have a parallel energy distribution. When the parallel energy of the primary electrons is lower than the absolute value of the potential barrier of the probe, the primary electrons cannot reach the probe surface, the number of the emitted electrons decreases. Hence, the absolute value of the total current also decreases. This decrease is not so rapid because of the particular properties of the parallel energy distribution of the primary electrons. Of course, in the mean time, the probe collects more-and-more ions, when the absolute value of the negative bias potential is increased. When the probe potential is sufficiently negative with respect to the plasma potential, all primary electrons are repelled and only ions are collected *(I)*, so the ion current also tends to saturate.

Theoretical model

We interpret in the following the foregoing results on the basis of a simplified theoretical model. We consider that the total electron current collected by the probe in the resonant zone consists of cold and hot electrons. In case of the probe used at the presented experiments, sheath dimensions were small compared to the probe dimensions. Therefore, it is convenient and adequate to use planar probe approximation to build the theoretical model.

In terms of Cartesian coordinates, we can write the probe current density of the electrons to the negatively biased probe as

$$j = e \cdot \int_{v_{z\,min}}^{\infty} \int_{-\infty}^{\infty} \int_{-\infty}^{\infty} f\left(v_x, v_y, v_z\right) \cdot v_z \, dv_x dv_y dv_z \tag{1}$$

where, minimal value of v_z from energy conservation is

$$v_{z\,min} = \left[2 \cdot e \cdot \left(V_{pl} - V_{pr}\right) / m_e\right]^{1/2} \tag{2}$$

and V_{pl} is the plasma potential, V_{pr} is the probe bias-voltage, m_e is the electron mass , and e is the magnitude of the electron charge. Assuming loss-cone distribution for the cold electron component [4]

$$f_c(v_{//}, v_\perp) = n_c \cdot \left(\frac{m_e}{2 \cdot \pi \cdot T_{c//}} \right)^{1/2} \cdot exp\left(- \frac{m_e \cdot v_{//}^2}{2 \cdot T_{c//}} \right) \cdot \frac{m_e}{2 \cdot \pi \cdot T_{c\perp} \cdot j!} \cdot \qquad 3)$$

where $T_{c//}$ and $T_{c\perp}$ are the parallel and perpendicular temperatures of the cold electrons, respectively (measured in energetic units), and n_c is the cold electron density, we obtain for the cold electron current density the following expression

$$\begin{aligned} j_c &= j_c^* \cdot exp\left[- \frac{e \cdot (V_{pl} - V_{pr})}{T_{c//}} \right], \qquad if \qquad V_{pr} \le V_{pl} \\ j_e &= j_e^* \qquad\qquad\qquad , \qquad if \qquad V_{pr} \ge V_{pl} \end{aligned} \qquad 4)$$

where $j_e^* = e \cdot n_c \cdot \sqrt{T_{c//} / 2 \cdot \pi \cdot m_e}$ is the cold electron saturation current density.

Electrons gain high energies in ECR ion sources due to the ECR effect [5]. The *B-minimum* type magnetic trap of the source, which is formed by the superposition of the axial and the multipole radial magnetic fields, confines these hot electrons. The hot electrons are confined by the multipole magnetic field in the direction perpendicular to the axis of the source; therefore we consider that the hot electrons are mono-energetic in this direction. However, we assume Maxwell-type distribution in the direction parallel to the source axis. The distribution function obtained this way is the Maxwell-ring distribution, which can be written for the hot electron component as

$$f_h(v_{//}, v_\perp) = \frac{n_h}{2 \cdot \pi \cdot w_\perp} \left(\frac{m_e}{2 \cdot \pi \cdot T_{h//}} \right)^{\frac{1}{2}} \delta(v_\perp - w_\perp) e^{-\frac{m v_{//}^2}{2 T_{h//}}} \qquad 5)$$

where $w_\perp$ is the common perpendicular velocity, n_h the electron density, and $T_{h//}$ the parallel temperature of the hot electrons. The expression of the current density of the hot electrons can be obtained substituting the Maxwell-ring distribution function into Eq.1.

$$j_h = e \cdot n_h \sqrt{\frac{T_{h//}}{2 \cdot \pi \cdot m_e}} \exp\left[-\frac{e \cdot (V_{pl} - V_{pr})}{T_{h//}} \right] \qquad 6)$$

To calculate the electron current density resulted due to the secondary electron emission of the probe, it is convenient to make use of the definition of the secondary electron emission coefficient (denoted by σ). This coefficient is defined as the ratio of the emitted to the incident current density and depends on the incident particle energy. Thus the secondary electron current density can be written as

$$j_s = -e \cdot \int\int\int v_z \cdot \sigma(\varepsilon_w) \cdot f(v_x, v_y, v_z) d^3 v \qquad 7)$$

where σ is evaluated at ε_w, which is the kinetic energy of the incident hot electrons at the probe. The minus sign indicates that the emission current appears as an apparent ion current.

The dependence of the coefficient σ on the primary electron energy is described by the semi-empirical formula given by [6]:

$$\sigma(\varepsilon_w) = (2{,}72)^2 \frac{\varepsilon_w}{E_{\max}} \sigma_{\max} \exp\left[-2 \left(\frac{\varepsilon_w}{E_{\max}} \right)^{\frac{1}{2}} \right] \qquad 8)$$

where E_{max} is the electron energy where the emission coefficient σ has its maximum yield σ_{max}.

Using cylindrical system of coordinates, the secondary electron current density can be written as:

$$j_s = -e \int_0^{2\cdot\pi} \int_0^{\infty} \int_{v_{z\min}}^{\infty} v_z \cdot a \cdot (\varepsilon + e \cdot U) \cdot \exp(-b \cdot \sqrt{\varepsilon + e \cdot U}) \cdot f(v_z, v_\perp) \cdot \qquad 9)$$

In the above expression we introduced the following notations,

$$a = (2{,}72)^2 \frac{\sigma_{\max}}{E_{\max}} \quad , \quad b = \frac{2}{\sqrt{E_{\max}}} \qquad 10)$$

and also considered, that the electron kinetic energy on the surface of the probe is given by

$$\varepsilon_w = \varepsilon + eU \tag{11}$$

where $U = V_{pr} - V_{pl}$ represents the potential difference between the probe and the plasma.

Inserting the Maxwell-ring distribution (5) in Eq.9., we obtain

$$j_s = -\frac{e \cdot n_h \cdot a}{\sqrt{2 \cdot \pi \cdot m_e \cdot T_{h//}}} \int_{-eU}^{\infty} (\varepsilon_{//} + E_{\perp} + eU) \exp\left[-b(\varepsilon_{//} + E_{\perp} + eU \right. \tag{12}$$

where $\varepsilon_{//} = m \cdot v_z^2 / 2$ is the electron energy corresponding to the motion parallel to the longitudinal magnetic field and $E_{\perp} = m \cdot w_{\perp}^2 / 2$ is the perpendicular electron energy.

The total current to the probe is the sum of the electron currents and the ion current. In the ECR plasma ($T_i << T_e$) the ion saturation current density is given by the Bohm current density [7]

$$J_i = -0.61 \cdot n \cdot e \cdot \sqrt{\frac{T_{eff}}{m_i}} \tag{13}$$

where we used an effective electron temperature taking into account that in the resonant zone there are two types of electrons present with different number density and temperature. The effective temperature can be defined as [8]

$$\frac{1}{T_{eff}} = \frac{n_c}{nT_c} + \frac{n_h}{nT_{h//}} \tag{14}$$

where $n = n_c + n_h$ is the total electron plasma density.

The total current density to the probe is given by the sum of the cold *(j_c)*, hot *(j_h)*, secondary *(j_s)* electron current density, respectively, and the ion current density *(j_i)*. Substituting the above determined expressions (4, 6, 12 and 13) into the sum

$$j = j_c + j_h + j_s + j_i \tag{15}$$

we obtain for the total current density the following expression :

$$j = e \cdot n_h \cdot \sqrt{\frac{T_{c//}}{2 \cdot \pi \cdot m_e}} \cdot \exp\left(\frac{e \cdot U}{T_h}\right) + e \cdot n_h \cdot \sqrt{\frac{T_{h//}}{2 \cdot \pi \cdot m_e}} \exp\left(\frac{e \cdot U}{T_{h//}}\right)$$

$$\cdot \int_{-eU}^{\infty} (\varepsilon_{//} + E_{\perp} + e \cdot U) \exp\left[-b \cdot (\varepsilon_{//} + E_{\perp} + e \cdot U) \cdot \exp(\varepsilon_{//} + E_{\perp} + \epsilon \right. \quad (16)$$

$$- 0.61 \cdot n \cdot e \cdot \sqrt{\frac{T_{eff}}{m_i}}$$

Calculated total current densities $j = j(n_c, n_h, T_c, T_{h//}, E_{\perp}, V)$ are shown in Fig.2. for various parameter combinations considering tungsten probe (E_{max} = *700 eV* and σ_{max} = *1,4*). The calculated curves have the same profile as the experimentally measured ones.

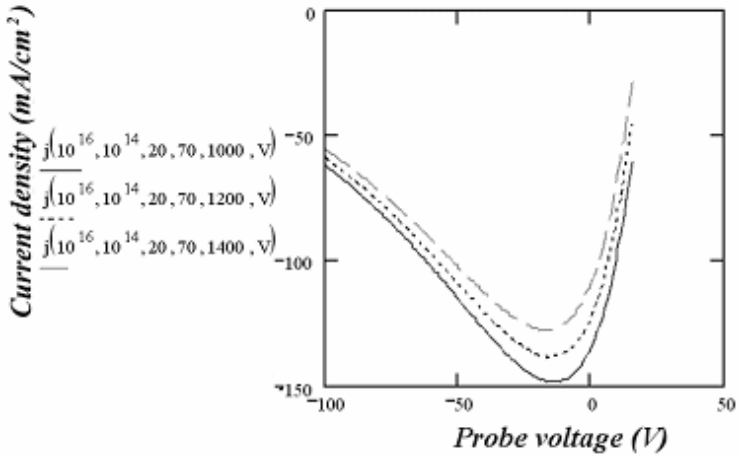

Fig. 2. Calculated total current density to the probe
Different hot electron energies, $E_{\perp} > E_{max}$

The curves on the Fig.2. are obtained for constant cold and hot electron densities, parallel temperatures, and different hot electron energies. We can conclude that increasing perpendicular energy of hot electrons determines the decrease of the observed current minimum, when $E_{\perp} > E_{max}$. We can explain this fact if we take into account the energy dependence of the secondary emission coefficient.

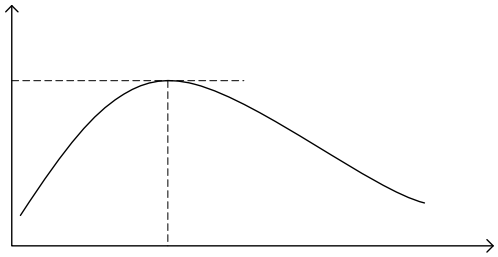

Fig. 3. Behavior of the secondary electron emission coefficient

Figure 3. shows the qualitative dependence of the secondary electron emission coefficient versus incident electron energy. This coefficient increases monotonously for most metals reaching a maximum value somewhat greater than 1 at incident energies of the order of several hundred *eV*-s *(E_{max})*. Further increase of the incident electron energy causes the reduction of the secondary emission.

When the hot electron energy increases above E_{max}, the number of the secondary electrons decrease and thus the absolute value of the total current will also decrease. This process can be observed on Fig.2. One can see that the change of the hot electron energy causes the shift, and also the magnitude change of the minimum of the probe voltage-current characteristics. This particular behavior is observed on the experimental curves, too. Departing from the resonant zone, the perpendicular energy of the hot electron will increase (mirror effect), which causes the decrease of the value of the total current observed at the minimum point on the experimental curves.

A series of curves corresponding to different parallel energies of the hot electrons are presented on Fig.4., all other parameters having constant values. One can see that the increase of the parallel temperature causes the minimum position to be shifted toward lower negative voltages.

When the probe is pulled away from the resonant zone, the minimum positions which are at negative voltages will shift towards smaller absolute voltage values. Due to the confinement mechanism of the mirror machines, as the probe departs from the resonant zone, the parallel velocity (temperature) of the hot electrons will decrease. The same conclusion can be drawn from the theoretical curves. In case of lower parallel energies, the minimum is obtained again at negative voltages with smaller absolute values.

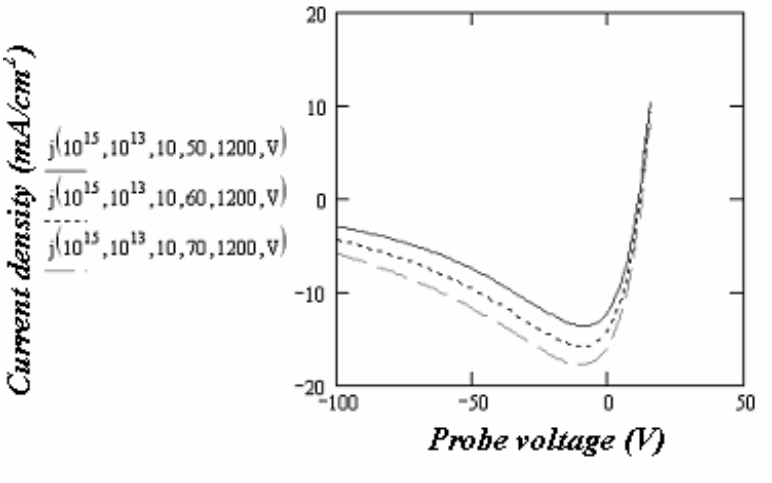

Fig. 4. Calculated total current density to the probe
Different parallel electron temperatures

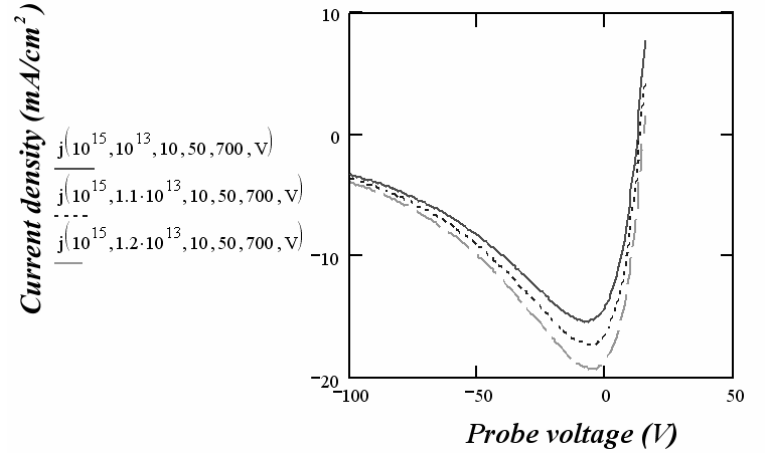

Fig. 5. Calculated total current density to the probe
Different hot electron density

The increase of the density of the hot electron (of course only in certain limits) also causes the increase of the absolute value of the minimum (Fig. 5). The same behavior can be observed on the experimental curves either. Departing from the resonant zone, the density of the hot electron decreases, which causes the decrease of the value of the total current observed at the minimum point on the experimental curves, too.

CONCLUSIONS

The goal of this paper was to give explanation for the appearance of the emphasized minimum observed in the ion current region of the probe voltage-current curve of a Langmuir-probe used in the hot regions of the ECR plasma. We assumed that this effect is due to the secondary electron emission of the probe material. Starting from a simplified hot electron distribution function, we deduced a formula for the total current density collected by the probe. Using computer codes of the theoretical model, we studied graphically the influence on the total current of the different plasma parameters. Our study showed that the shape of the curves resulted from our model is in agreement with the experimental curve shapes. This means our assumption was correct, the secondary electron emission of the probe is the mechanism, which causes the apparition of the unusual shaped voltage-current characteristics. Further investigations are needed to fit our model to the experimental curves and determinate local plasma parameters of the hot ECR plasma.

Acknowledgement

Among the authors L. K. was supported by the Domus Hungarica Scientarium et Artium Fellowship, the Arany János Foundation and the Hungarian Ministry of Education, and J.K. was supported by the Domus Hungarica Scientarium et Artium Fellowship.

REFERENCES

1. L. Kenéz et al., Nucl. Instrum. Methods Phys. Res. B *187/2* (2002) 249
2. L. Kenéz et al., Rev. Sci. Instrum. *73/ 2* (2002) 617
3. S. Biri, J. Vámosi, Proc. 11th Inte. Workshop on ECRIS, Groningen, (1993) KVI-Report 996, 128
4. R.A.Dory, G.E.guest, E.G.Harris, Phys.Rev.Lett.14,(1965) 131
5. R. Geller, Electron Cyclotron Resonance Ion Sources and ECR plasmas, IOP Publ. Ltd (1996)
6. K. Ertl, R. Behrisch, in Physics of Plasma-Wall Interaction in Controlled Fusion, (ed. D.E. Post, R. Behrisch), Plenum Press, New York, (1986) 515
7. D.Bohm, in "The Characteristics of Electrical Discharges in Magnetic Fields (A.Guthrie and R.K.Wakerling,eds) Mc Graw-Hill, New York, (1949)
8. P.C. Stangeby, Nucl. Mater. 128-129, (1984) 969

STUDIA UNIVERSITATIS BABEŞ BOLYAI, PHYSICA, L, 1, 2005

SPECTRAL TITRATION OF THE PROTEORHODOPSIN

KLÁRA MAGYARI*, MELINDA LAKATOS‡, JULIÁNNA SZAKÁCS+, GYÖRGY VÁRÓ†

* *Babeş-Bolyai University, Faculty of Physics, Cluj-Napoca, Romania;*
† *Institute of Biophysics, Biological Research Center of the Hungarian Academy of Sciences, Szeged, H-6701 Hungary;*
+ *Department of Biophysics, University and Pharmacy, Tg. Mures, Romania*

ABSTRACT. Proteorhodopsin is a retinal-containing integral membrane protein. It is a light-driven proton pumping whit a photocycle similar to that of bacteriorhodopsin. The pK_a of the wild-type PR was determined from spectral titration in the pH range 4.5-10. The pK_a of the proton acceptor Asp-97 was established to be 7.1. Comparing this value with the pK_a of the proton acceptor group of bacteriorhodopsin, being 2.5, the proteorhodopsin has a much higher pK_a. The potential importance of proteorhodopsin is in the possible applications in optical data storage and optical signal processing.

INTRODUCTION

Recently, large numbers of new retinal proteins were discovered in both prokaryotic and eukaryotic organism. They could be classified in two clearly distinct families: type 1, the archaeal-type rhodopsin and, type 2, the photosensitive receptor proteins (Spudich et al., 2000). Proteorhodopsin, a light-driven proton pump belongs to the retinal protein family type 1. It was discovered in the uncultivated marine γ-bacteria of the SAR 86 (Beja et al., 2000, Beja et al., 2001). Its relatively simple structure makes easier to study this protein. The function of the proteorhodopsin is similar to that of bacteriorhodopsin. Upon light excitation electrical potential difference appears between the two surfaces of the cell membranes, due to an active proton transport across the membrane.

Similar to other retinal proteins, the proteorhodopsin is formed from seven transmembrane α-helices. The early studies suggested that the chromophore in the protein is an all-*trans* retinal bound covalently to a lysine in helix G via a protonated Schiff base (Beja et al., 2000). After light excitation the retinal photoisomerizes to 13-cis, and a photocycle is initiated. During the photocycle a proton is transported across the cell membrane from the cytoplasm to the extracellular space. The amino acid sequence, the deduced structure of the seven transmembrane helices, the transport functions and the photocycle of proteorhodopsin at high pH (Váró et al., 2003) all show great similarities to that of bacteriorhodopsin.

A comparative study of the two sequences and FTIR measurements identified the putative proton acceptor and donor sites in the proteorhodopsin, as Asp-97 and Glu-108 respectively (Lakatos et al., 2003, Dioumaev et al., 2002).

In bacteriorhodopsin, the pK_a of the proton acceptor Asp-85 is 2.5 (Balashov et al., 1996). If the pH is bellow this pK_a a proton is bound to the acceptor and can not bind another proton, the transport is blocked (Váró and Lanyi, 1989, Dér et al., 1991). In this paper we describe the spectral titration of the Asp-97, the proton acceptor site of the proteorhodopsin and determine its pK_a.

MATERIALS AND METHODS

Wild-type proteorhodopsin was expressed in *Escherichia coli* (strain UT5600), as described before (Beja et al., 2000; Dioumaev et al., 2002). The cells were broken using an Aminco French press at 12 Mpa. The membranes were purified by centrifugation in distilled water and on a sucrose gradient.

For measurements acrylamide gel samples were prepared according to a procedure described elsewhere (Mowery et all, 1979). During the sample preparation no buffer or salts was used to avoid the aggregation of the membranes. The gels were equilibrated with a bathing solution containing 100 mM NaCl, 25 mM MES (2-[N-morpholino]ethanesul-fonic acid) and 25mM TRIS (Tris[hydroxymethyl]aminomethane) buffer. The pH of the samples was adjusted between 4 to 10 whit HCl and NaOH, and the temperature of the sample was kept constant at 20˚C. The spectra were measured with a computer controlled Unicam UV/Vis spectrometer.

RESULTS AND DISCUSSION

As reported before (Dioumaev et al., 2002), the spectrum of proteorhodopsin shifted from 546 nm to 517 nm whit increasing pH due to titration of the proton acceptor site of the protein. The pK_a of the wild-type proteorhodopsin was established from spectral titration in the pH range 4.5-10.

The studies published so far suggest that the spectral changes of the proteorhodopsin are very similar to those of the bacteriorhodopsin. Taking this as a basis we determined the titration curve using the amplitude changes in the difference spectra (Fig. 1). The pH in the range of 4 to 10 was adjusted and the sample kept overnight to equilibrate. The spectra were taken between 350 and 700 nm. The data were stored and processed in computer. The difference spectra (Fig. 1) were obtained after subtracting the spectrum measured at pH 4 from the others. By analyzing the difference spectra it can be observed the appearance of an absorption maximum at 500 nm and a minimum at 570 nm. The calculated difference amplitudes yield the points for the titration curve (Fig. 2). They were fitted with the Henderson-Hasselbalch equation, which results an inflection point at pH 7.1, the value of the pK_a for the proteorhodopsin.

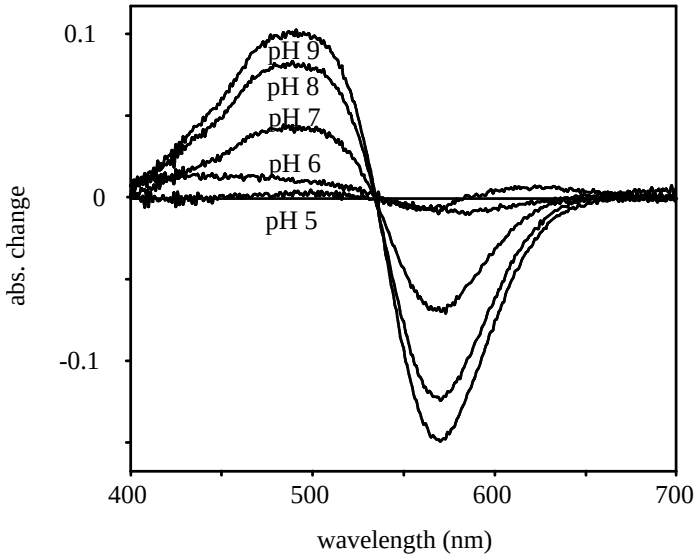

Fig. 1. The difference spectra of the proteorhodopsin, after subtracting the spectrum at pH 4 from the others. Measuring conditions: 20^0C, 100 mM NaCl, 25 mM MES and 25 mM TRIS in the pH range 4-10

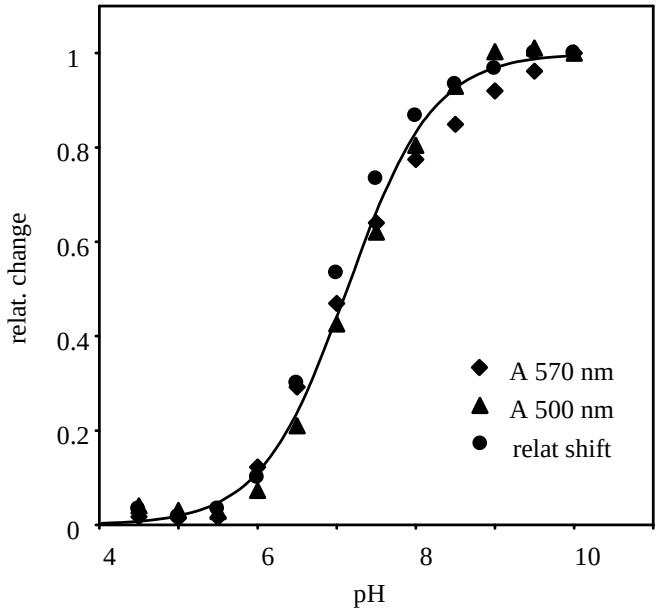

Fig. 2. The relative change of the amplitude at 500 nm and 570 nm and the fitted titration curve. The apparent pK_a is 7.1.

If the samples were kept at room temperature for several days, the measured pK_a shifted toward higher pH values (Friedich et al., 2002). Presumably this is caused by oxidation of one or more of the three cysteine in the protein (Lakatos et al., 2003). To avoid this problem, we used freshly prepared samples for determination of the pK_a.

Comparing the proteorhodopsin with other retinal protein this value seems high. The proteorhodopsin as a proton pump functions similarly to the bacteriorhodopsin only above this pH. If the pH is lower than 7.1, the proton acceptor is not available, the retinal Schiff base can not deprotonate and the transport is blocked (Lakatos et al., 2003).

REFERENCES

1. Balashov, S. P., E. S. Imasheva, R. Govindjee, and T. G. Ebrey. 1996. Titration of aspartate-85 in bacteriorhodopsin: What it says about chromophore isomerization and proton release. *Biophys. J. 70:473-481*
2. Beja, O., L. Aravind, E. V. Koonin, T. Suzuki, A. Hadd, L. P. Nguyen, S. B. Jovanovich, and E. F. DeLOng. 2000. Bacteriorhodopsin: evidence for a new type of phototrophy in the sea. *Science. 289:1902-1906*
3. Beja, O. E. N. Spudich, J. L. Spudich, M. Lecrerc, and E. F. DeLong. 2001. Proteorhodopsin phototropy in the ocean. *Nature. 411:786-789*
4. Dér, A., R. Tóth-Boconádi, and L. Keszthelyi. 1989. Bacteriorhodopsin as a possible chloride pump. *FEBS Lett. 259:24-26*
5. Dioumaev, A. K., L. S. Brown, J. Shih, E. N. Spudich, J. L. Spudich and J. K. Lanyi. 2002. Proton transfer in the photochemical reaction cycle of proteorhodopsin. *Biochemistry. 41:5348-5358*
6. Friedrich, T., S. Geibel, R. Kalmabach, I. Chizhov, K. Ataka, J. Heberle, M. Engelhard, and E. Bamberg. 2002. Proteorhodopsin is a light-driven proton pump whit variable vectoriality. *J. Mol. Biol. 321:821-838*
7. Melinda Lakatos, Janos K. Lanyi, Juliánna Szakács and György Váró. 2003. The photochemical reaction cycle of proteorhodopsin at low pH. *Biophys. J. 84: 3252-3256*
8. Spudich, J. L., C. S. Yang, K. H. Jung, and E.R. Spudich. 2000. Retinyline proteins: structures and functions from archea to humans. *Annu. Rev. Cell Dev. Biol. 16:365-392*
9. Váró Gy., L. S. Brown, M. Lakatos and J. K. Lanyi. 2003. Characterization of the photochemical reaction cycle of proteorhodopsin. *Biopys. J. 84: 1202-1207*
10. Váró Gy., and J. K. Lanyi.1989. Photoreactions of bacteriorhodopsin at acid pH. *Biophys. J. 56:1143-1151*

STUDIA UNIVERSITATIS BABEŞ BOLYAI, PHYSICA, L, 1, 2005

DIRECT MICROWAVE ABSORPTION INVESTIGATION OF THE $YBa_2Cu_3O_{7-\delta}$:Li SUPERCONDUCTOR SYSTEM

M. VELTER-STEFANESCU[a], O.G. DULIU[b], V. SANDU[a], I. URSU[b]

[a]National Institute of Materials Physics, Magurele, P.O. Box MG-7, RO-077125 Bucharest, Romania
[b]University of Bucharest, Department of Atomic and Nuclear Physics, Magurele, P.O. Box MG-11, RO-077125 Bucharest, Romania

ABSTRACT. Neutron irradiated Li (2 at. %.) doped $YBa_2Cu_3O_{7-\delta}$ system has been investigated by direct microwave absorption. After irradiation, the superconducting properties of the 123 phase were modified depending on the neutron fluency. Increasing the fluency, the phase structure supports initially a disordering, then a re-ordering accompanied by a significant increase of the average critical temperature T_c after 5 10^{17}cm^{-2} irradiation; at the highest fluency (10^{18}cm^{-2}) T_c decreases denoting the degradation of the 123 the phase. The intragranular dephasing magnetic field B_d, i.e. the DMA parameter associated with the magnetic field dependence of the critical current density, reflects the evolution of the material structure, initially decreasing after first irradiation (5 10^{17}cm^{-2}) and then increasing at higher fluencies. Another interesting peculiarity, consisting of the presence of a flatness of the DMA curves around 0.5 T, and that exists only in irradiated samples, was interpreted as a peak effect.

Key words: Direct microwave absorption, High temperature superconductivity, peak effect

1. INTRODUCTION

Among the methods intensively used to investigate the high-Tc superconductors (HTcS), as standard transport and magnetic measurements, or by the microwave alternative technique, as magnetically modulated microwave absorption (MAMMA) [1, 2], the direct microwave absorption (DMA) [3] remarks themselves by simplicity and, at the same time, the amount of information they can provide.

DMA characteristic curves, that illustrate the dependency of microwave absorption versus steady magnetic, have habitually an incomplete inverse bell shape whose minimum corresponds to zero value of dc-magnetic field. The asymptotical values of the DMA signals (considered in this work as conventional "zero" reference levels of the corresponding DMA responses) correspond to the

maximum microwave absorption in sample. The typical DMA curve for bulk samples shows a fast rising (FR) section of the microwave absorption, usually within 0 to 40 mT magnetic field range, followed at higher field values by a slow rising (SR) section (Fig. 1). As showed in [3], the decoupling of the intergranular Josephson junctions (JJ's) by the external dc-magnetic field generates the FR, while SR behaviour is related to the contribution of the intrinsic weak links from inside the grains. The last one is the most significant section of DMA curve as it can furnish information concerning the superconducting phase within the material itself. Accordingly, this region can be very well described by a simple exponential law [3]:

$$Y = |Y_0| \exp\left(-\frac{B}{B_d}\right) \tag{1}$$

where: Y represents the SR DMA signal, Y_0 is the maximum value of the SR DMA signal corresponding to zero-magnetic field and reflects the superconducting phase quantity and B stands for the magnetic field, while B_d represents the intragranular dephasing magnetic field, tightly correlated with the intragranular critical current density [3, 4]. Another important parameter of DMA curve is the zero magnetic field value of the FR section, Y_{0j}, directly connected to the intergranular JJ's number. Its value has been determined by subtracting the Y_0 amplitude (obtained by a best fit method) from the experimental DMA curves in the region of zero dc-magnetic fields.

In this way, DMA represents a complementary method that allows the estimation of the intergranular JJ's quantity, Y_{0j}, as well as the extent of superconducting phase, Y_0, and the values of intragranular dephasing magnetic field, B_d. Applied to neutrons irradiated samples, this method is very useful in characterising the influence of heavily ionising radiation onto the HT_cS. Accordingly, in the present paper we report the results of our studies by direct microwave absorption (DMA) on the neutron irradiated Li (2 at. %.) doped $YBa_2Cu_3O_{7-\delta}$ system.

2. MATERIALS AND METHODS

2.1 SAMPLES

Polycrystalline samples of the $YBa_2Cu_3O_{7-\delta}$:Li (2 at. %) system were prepared by the conventional solid-phase reaction from a mixture of high-purity starting materials Y_2O_3, CuO and $BaCO_3$. Li was introduced by adding of LiOH. For this purpose, appropriate amounts of these materials were calcinated at 930 ^{0}C for 20 hours in flowing oxygen. Regrinding, pelletization and a final sintering under the same conditions completed the process [5]. Previous investigations [6] showed that the samples are single phase orthorhombic $YBa_2Cu_3O_{7-\delta}$, with an important amount of large (<100 μm) and well matched grains (like the bricks in a wall).

2.2 IRRADIATION

The irradiation with thermal neutrons was performed at the VVRS nuclear reactor of the National Institute for Physics and Nuclear Engineering-Bucharest at the following fluencies: $10^{17}cm^{-2}$, 5 $10^{17}cm^{-2}$ and $10^{18}cm^{-2}$. During irradiation, the sample temperature was maintained below 40 ^{0}C by using an appropriate cooling system.

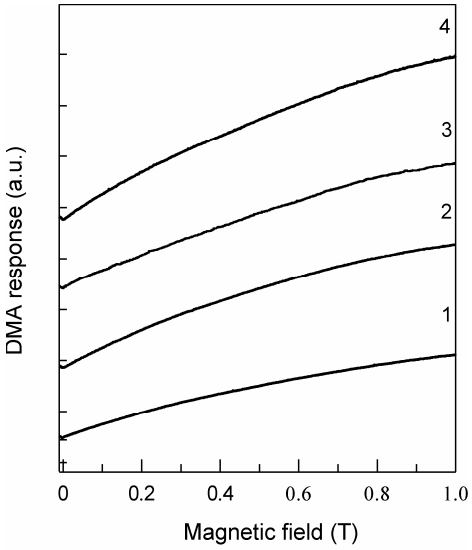

Fig. 1. The experimental DMA curves of the $YBa_2Cu_3O_{7-\delta}$:Li (2 at %) system, before (1) and after the thermal neutron irradiation at: $10^{17}cm^{-2}$ (2), 5 $10^{17}cm^{-2}$ (3) and respectively $10^{18}cm^{-2}$ (4) fluencies.

2.3 DMA MEASUREMENTS

The microwave absorption investigations by DMA method were carried out with an on-line, X-band (9 GHz) home-made spectrometer, at an incident microwave power of the 3 mW. The magnetic field induction has been monitored by the means of a digital teslameter with an average precision of 0.1 mT.

DMA experiments were performed at 77 K, by sweeping slowly the steady magnetic field from -15 mT to 1 T in 2 min. All the time the sample has been placed in the maximum of the microwave magnetic field. More details concerning experimental set-up, spectrometer sensitivity and measurements reproducibility have been previously described in ref. [3-5]. Further, the signal amplitudes were reported at the same amplification and at the same sample quantity, *i.e.* 10 mg.

3. RESULTS AND DISCUSSION

The experimental DMA curves are reproduced in Fig.1, while the numerical values of corresponding parameters: zero-magnetic field FR (Y_{0j}) and SR (Y_0) amplitudes, as well as the intragranular dephasing magnetic field B_d (determined using a best-fit method) are given in Table 1. In interpreting of the

experimental data, it must be taken into account the fact that the concentration of neutrons induced defects monotonously increases with the neutron fluency.

A careful analysis of the DMA curves of all irradiated samples shows the same peculiarity: flatness in the microwave absorption around 0.5 T that in fact represents a small deviation from the exponential law of the SR described by eq. 1. In order to evidence clearly this effect, we subtracted from the experimental curves the exponential ones as determined from the fit of the experimental data at magnetic fields lower than 0.15 T and higher than about 0.7 T (Fig. 2). At all irradiated samples we have noticed the presence of this peak whose amplitude is strongly influenced by the neutron fluencies. Its area increases monotonously with the neutron fluency and reaches its maximum for 5 10^{17} cm^{-2}.

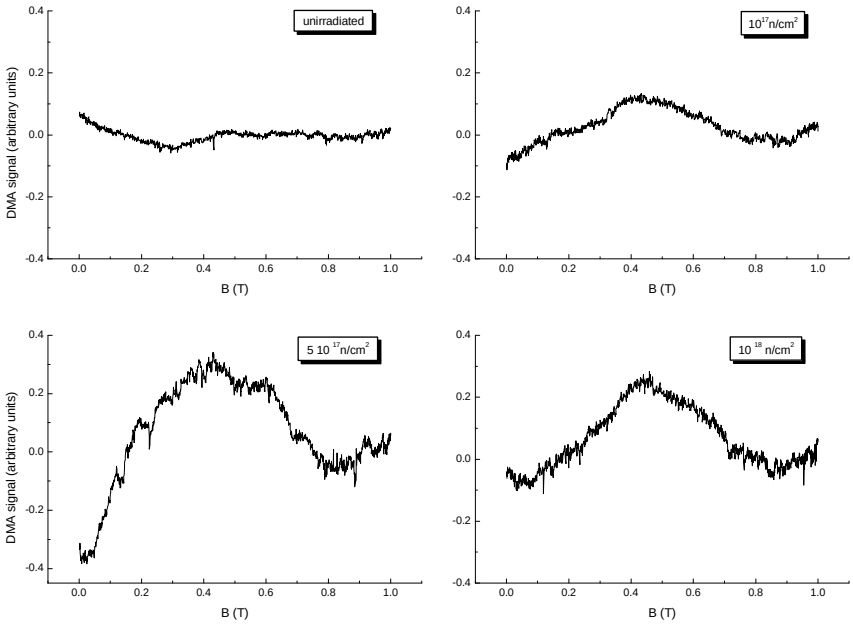

Fig. 2. The SR peaks of the $YBa_2Cu_3O_{7-\delta}$:Li (2 at. %) samples

The variation of the dephasing magnetic field (B_d) reflects very well the evolution of the phase structure: it decreases after $10^{17}cm^{-2}$ fluency, when 123-phase was disordered and recovers almost at the initial value for 5 $10^{17}cm^{-2}$, which led to a well organised 123-phase (Table 1). At the same time, the density of intergranular JJ's maintains a very low and nearly insensitive value to irradiation, in total agreement with the MAMMA investigations [5].

The experimental data concerning both SR peak area and Y_0 parameters support the initial assumption made on the basis of MAMMA results that certain initially non-superconducting intergranular zones were activated at T > 77 K by irradiation. Some of such zones, with T_c closed to 77 K, can act as efficient intragranular pinning centres if the steady magnetic field normalises them [7], determining, in this way, the slow growth of intragranular dephasing magnetic field B_d after the highest fluencies (Table 1).

It must be emphasis that the SR peaks reflect the usual peak effect described in ref. [8-16]. Such peaks mark the role of the surface as a source of pre-irradiative defects that constitute accumulation centres for the point defects generated during irradiation. By increasing the magnetic field, the small zones containing clusters of point defects coalesce together and become pinning centres.

Table 1.

The MAMMA [5] and DMA parameters of the $YBa_2Cu_3O_{7-\delta}$:Li (2 at. %) samples before (1) and after the thermal neutron irradiation at $10^{17}cm^{-2}$ (2), 5 $10^{17}cm^{-2}$ (3) and 10^{18} cm^{-2} (4) fluencies.

Sample		MAMMA		DMA		
		T_c^{mw} (K)	ΔT_c^{mw} (K)	Y_{0j} (a.u.)	Y_0 (a.u.)	B_d
$YBa_2Cu_2O_{7-\delta}$ (2 at. % Li)	1	84.3	> 3.0	0.07	9.0	1.02 ± 0.05
	2	83.1	< 3.0	0.08	11.9	0.79 ± 0.03
	3	85.7	2.3	0.10	13.1	0.96 ± 0.03
	4	81.3	4.0	0.05	17.1	0.96 ± 0.03

- a.u. stands for arbitrary units.

4. CONCLUDING REMARKS

Sintered samples of Li (2 at. %) doped $YBa_2Cu_3O_{7-\delta}$ have been irradiated at room temperature with thermal and epithermal neutrons. The pecularities of the irradiative changes induced on the 123 phase evidenced by direct microwave absorption (DMA) method are presented and discussed. After irradiation, the superconducting properties of the 123 phase were modified depending on the neutron fluency. Increasing the fluency, as evidenced by previous MAMMA study [5]: the phase structure supports initially a disordering, then a re-ordering accompanied by a significant increase of the average critical temperature after 5 $10^{17}cm^{-2}$ irradiation; at the highest fluency ($10^{18}cm^{-2}$) the T_c^{mw} decreases denoting the degradation of the 123 the phase. The intragranular dephasing magnetic field

B_d, the DMA parameter associated with the magnetic field dependence of the critical current density, reflects the evolution of the structure, with a decrease after first irradiation ($5\ 10^{17} cm^{-2}$) followed by an increase at higher fluencies. Another interesting peculiarity is the presence of a flatness of the DMA curves around 0.5 T that manifests only in irradiated samples, interpreted by us as a peak effect.

Acknowledgement: This work has been performed within CERES, nr 78/2002 project

REFERENCES

1. K. Moorjani, J. Bohandy, F.J. Adrian, B.F. Kim, R.D. Shull, C.K. Chiang, L.J. Schwartzendruber, L.H. Bennet, Phys. Rev. B **36,** 4036, (1987).
2. Shaltiel D, Bill H, Grayevsky A,Junod A, Lovy D, Sadowsky W, Walker E, Phys. Rev. B **43**, 13594, (1991,).
3. M. Velter-Stefãnescu, M. Bastea, Rom. J. Phys. **38,** 797, (1993).
4. M. Velter-Stefãnescu, A. Totovânã, A. Novac, Rom. J. Phys. **39,** 585, (1994).
5. M. Velter-Stefãnescu, A. Totovânã, V. Sandu, J. Supercond. **11**, 327, (1998).
6. V. Sandu, J. Jaklovszky, E. Cimpoiasu, M.C. Bunescu, J. Supercond. **10,** 231, (1997)
7. M. Däumling, J.M. Seuntjens, D.C. Larbalestier, Nature **346**, 332, (1990).
8. V.V. Moschalkov, A.A. Zhukov, I.V. Gladyshev, S.N. Gordeev, G.T. Karapetrov, V.D. Kusnetsov, V.V. Metlushko, V.A. Murashov, V.I. Voronkova, V.K. Yanovskii, J. Magn. Magn. Mater. **90-91,** 611, (1990).
9. T. Kobayashi, Y. Nakamura, K. Kishio, T. Kimura, K. Kitazawa K. Yamafuji, Appl. Phys. Lett. **62,** 1830, (1993).
10. L. Klein, E.R. Yacoby, Y. Yeshurun, A. Erb, G. Müller-Vogt, V. Breit, H. Wühl, Phys. Rev. B **49,** 4403, (1994).
11. S. Senoussi, F. Mosbah, K. Frikach, S. Hammond, P. Manuel, Phys. Rev. B **53** 12321, (1996).
12. A.A. Zhukov, H. Küpfer, G. Perkins, L.F. Cohen, A.D. Caplin, S.A. Klestov, H. Claus, V.I. Voronkova, T. Wolf, H. Wühl H, Phys. Rev. B **51,** 12704, (1995).
13. A. Erb, J-Y. Genoud, F. Marti, M. Däumling, E. Walker, R. Flükiger, J. Low. Temp. Phys. **105,** 1023, (1996).
14. A. Erb, J-Y. Genoud, M. Dhale, E. Walker, R. Flükiger, Physica C **282-287,** 2145, (1997).
15. Y. Kodama, K. Oka, Y. Yamaguchi, Y. Nishihara, K. Kajimura, Phys. Rev. B **56,** 6265, (1997).
16. S. Kwok, Physica B **197,** 579, (1994).

THE PRODUCTION OF ^{64}Cu FOR PET EXPERIMENTS

L. DĂRĂBAN, R. ADAM-REBELEŞ

Babes Bolyai University, Faculty of Physics
Kogălniceanu 1, RO-400084 Cluj-Napoca, Romania

ABSTRACT. Positron Emission Tomography (PET) is a new technique in medical imagery. This technique is based on simultaneous detection of 511 keV gamma annihilation radiations.

This annihilation radiation is generated by annihilation of a positron wich came from a β^+ radioisotope. Using a Am-Be, Pu-Be neutron source we produce β^+ isotopes with a longer half life. We try to use ^{64}Cu, ^{62}Cu produced radioisotopes in a $\gamma-\gamma$ coincidence assemblage. This assemblage is the base of Positron Emission Tomography.

1. Introduction

The β^+ radioisotopes currently used in medical imagery are: ^{11}C, ^{18}F, ^{13}N, ^{15}O. They have a half life time between 2 and 110 minutes. PET imagery is focusing on production of short live β^+ radioisotopes like ^{13}N, ^{15}O, [1].

Other β^+ radioisotopes were investigated in order to discover the advantage of applying them in medical imagery. In nuclear medicine, if a radionuclide disintegrates in other mode than β^+ it is necessarily that β^- or γ emitted energy to be very low.

2. Production of ^{64}Cu isotope

The reaction of cooper with neutrons can be written using the next formula:

$$^{63}Cu + ^{0}_{1}n \rightarrow ^{64}Cu + \gamma \qquad (1)$$

The cross section for thermal neutrons for ^{63}Cu is 4. 5 barni, [2].
In Fig. 1 we notice ^{64}Cu decay scheme:

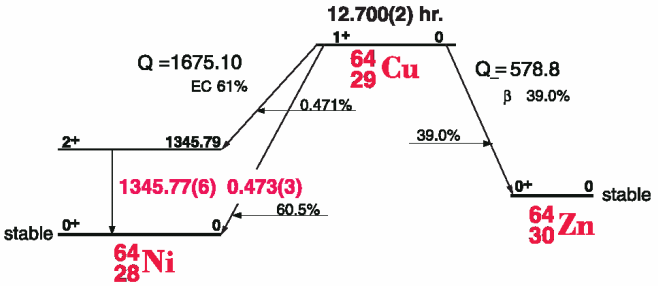

Fig. 1. ^{64}Cu decay scheme[3].

It can be seen that this radioisotope has a 12. 7 hours half time and it disintegrates both β^+ and β^-. The β^+ spectra have a maximum at 578. 7 keV, and average β^- energy of 67 keV, [2].

We use thermal neutron from ^{241}Am-^{9}Be, ^{239}Pu-^{9}Be sources ($\sim 10^6\ n/s \cdot cm^2$-fluence) for the production of ^{64}Cu isotope. Some Cu sample (optical spectrometry purity) were irradiated the for 6 hours and we recorded the γ spectra in 5 minutes. The gamma spectra of ^{64}Cu is represented in Fig. 2.

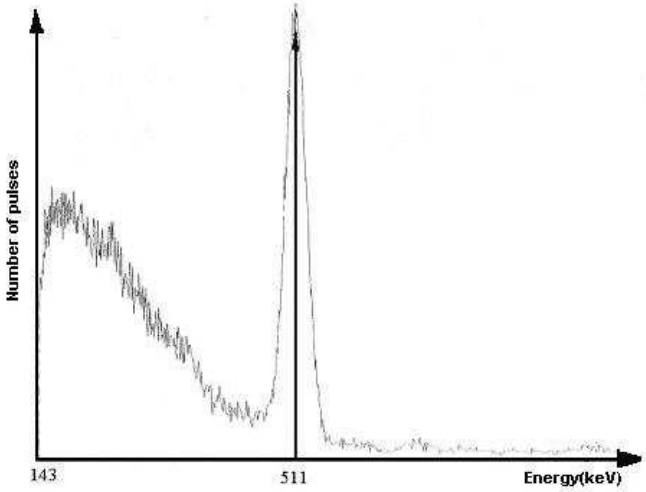

Fig. 2. ^{64}Cu γ spectra

We can be seen the presence of 511 keV annihilation peak so it is certainly that the probe contains ^{64}Cu. This radioisotope was applied to an PET experiment.

3. Theoretical problem of coincidence measurements

Suppose that we have a radiation source that emits β^+ and we want to determine the source activity by coincidence measurements. (see Fig 3)

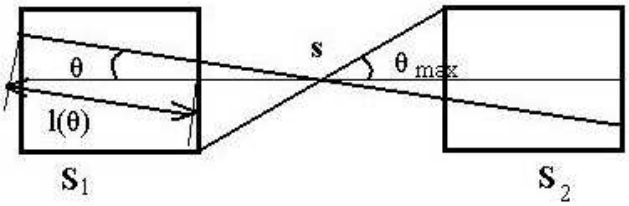

Fig. 3. Theoretical coincidence measurements

The assemble of detection consists in 2 identical NaI(Tl) scintillating crystals (S_1 respectively S_2). In this case the counting speeds on every channel of detection are [4]:

$$R_1^{'} = g_1 \varepsilon_1 \Lambda_1 \tag{2}$$

$$R_2^{'} = g_1 \varepsilon_2 \Lambda_2 \tag{3}$$

And the counting speed of real coincidences is donne by:

$$R_{12a} = g_{12} \varepsilon_{12} \Lambda_e \tag{4}$$

If measurement time is much shorter than half life time then the activity of the nuclid is:

$$\Lambda = \frac{\left(R_1 T_m - R_{f1} T_m\right)\left(R_2 T_m - R_{f2} T_m\right)}{R_{12a} T_m^{\ 2}} = \frac{\left(N_1 - N_{f1}\right)\left(N_2 - N_{f2}\right)}{N_{12a} Tm} \tag{5}$$

By counting the number of coincidence N_{12} corresponding to counting speed R_{12}, we can determine the real number of coincidences. (τ_r is the response time of assemblage, T_m measurement time) [1].

$$\begin{aligned} N_{12} &= N_{12a} + \frac{2\tau_r}{T_m}\left(N_1 - N_{12a}\right)\left(N_2 - N_{12a}\right) = \\ &= N_{12a}\left[1 - \frac{2\tau_r}{T_m}\left(N_1 + N_2\right)\right] + \frac{2\tau_r}{T_m} N_1 N_2 + \frac{2\tau_r}{T_m} N_{12a}^{\ 2} \end{aligned} \tag{6}$$

Because $N_{12a} << N_1, N_2$ we can ignore the $N_{12a}^{\ 2}$ term.

Than we have:

$$N_{12a} \approx \frac{N_{12} - \frac{2\tau_r}{T_m} N_1 N_2}{1 - \frac{2\tau_r}{T_m}\left(N_1 + N_2\right)} \tag{7}$$

In PET analysis this formula is useful for calculate the real number of measured coincidences. This formula is applied for every investigated point and finally it is obtained the real image of investigated organ. [5]

4. PET measurements

The PET assemblage consists in 2 detectors with NaI(Tl) scintillating crystals.

In a middle of these two detectors we put a ^{22}Na source, more strong as our ^{64}Cu with an 60 cm distance between detectors. For first experiment and the installation calibration we used a ^{22}Na source and not ^{64}Cu because ^{22}Na has a half

life time of 2. 6 years much longer then time of measurements and also, it is not necessarily to correct the loss of activity during measurements (the measurements take up to 2 hours and $T_{1/2}$ for ^{64}Cu is 12. 7 hours).

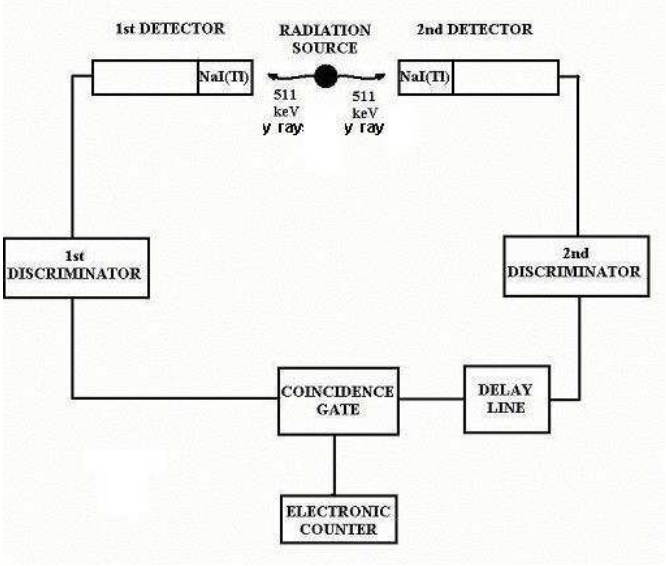

Fig. 4. $\gamma - \gamma$ coincidence assemblage

After the radiation is detected by the NaI(Tl) scintillating crystals, the electric signal corresponding to it goes to a discriminator, wich permits the pass only of an interval of voltage, corresponding on a specific energy. We obtain the γ spectra using short intervals of voltage window of 0. 2 V. So we obtained that the 511 keV peak energy is located between 2. 7 V and 3. 7 V.

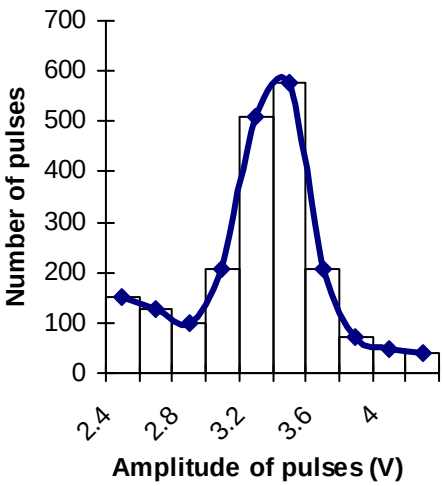

Fig. 5. *Radiation from annihilation of positrons using short intervals of voltage*

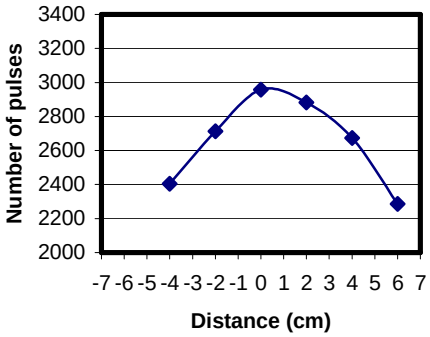

Fig. 6. Varying of coincidences with the source position

If the source is moved between these two detectors we obtain a curve with a maximum in a central zone. This curve has to be modified because of varying of the solid angle when moving the radiation source between the detectors.

For that we count the 511 keV pulses from every detector in different points and we obtain the variation of the detected annihilation rays with the solid angle. The measurements take 30 seconds for every investigated point.

After that we applied the next correction formula:

$$N_{real} = N_{masurat} - k(N_1 + N_2) \tag{8}$$

After appling this formula for every experimental point and fitting these points by a Gaussian curve it is obtained an almost perfect concordance between the experimental points and the approximation curve in the central zone, Fig. 8.

By measuring the FHWM we obtain a value of 4. 5 cm. This is the spatial resolution of the assemblage.

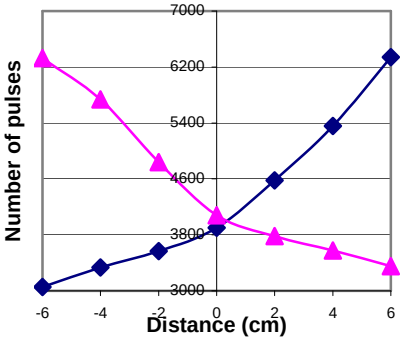

Fig. 7. The varying of the detected annihilation rays with the solid angle for every detector

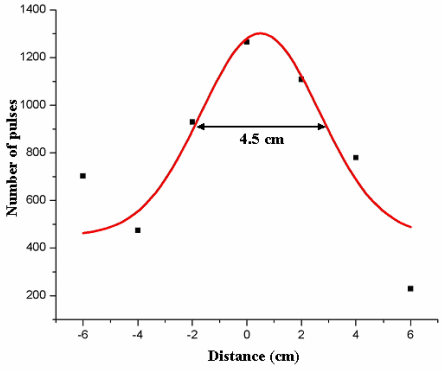

Fig. 8. Spatial resolution of the PET assemblage

5. Conclusions:

– The advantage of β^+ radioisotopes is that these radioisotopes can be used also in scintigraphy. It is only necessary to calibrate the peak energy for 511 keV corresponding to γ annihilation radiation

– We produced ^{64}Cu radioisotope was produced using thermal neutrons from isotopic neutron sources. The maximum activity induced is approximately 0. 5 μCi.

– Cooper is in a lower toxicity class than ^{99m}Tc, currently used in scintigraphic imagery.

– Using our PET assemblage with a ^{22}Na source we determine the position of the source with a precision of 4. 5 cm (FHWM) and delay between the annihilation signals was 6 μs.

REFERENCES

1. Mark Lubberink, *Quantitative Imaging with PET*, Disertation from Faculty of Medicine , 1032, Upsala p. 15, 17. (2001)
2. S. F Mughabghab, M. Divadeenam and N. E. Holden, *Neutron Cross Sections from Neutron Resonance Parameters and Thermal Cross Sections*, Academic Press (1981)
3. R. B. Firestone and L. P. Ekström, *"Periodic Table linked to decay data for known isotopes of each element"*, catalog, (2004).
4. A. Berinde, M. Grecescu, Probleme rezolvate de tehnica nucleara, p. 32, Ed. Tehnica, Bucuresti (1967)
5. Eric Harrah, *Hardware Design of PET Backprojection Algorithm using FPGA Technology, Thesis Master Degree,* Univ. of Tennessee, Knoxville, p. 3 (2002)

STUDIA UNIVERSITATIS BABEŞ BOLYAI, PHYSICA, L, 1, 2005

AN ALTERNATIVE METHOD FOR DATA ANALYSIS INVOLVED IN GAMMA SPECTROMETRY

D. FULEA[*], C. COSMA[**]

**Institute of Public Health "Prof. Dr. Iuliu Moldovan", Cluj-Napoca, Romania*
***Faculty of Physics, Babes-Bolyai University, Cluj-Napoca, Romania*

ABSTRACT. This paper presents an alternative method for efficiency and resolution calibration of the gamma systems. Based on the best algorithms of two data acquisition softwares (Assayer provided by Canberra Company and Gamma 2000 provided by Silena Company), quantitative gamma analysis was also made. These softwares are frequently used in the specific laboratories.

The measurements were performed on two gamma NaI(Tl) analyzers. Both systems contain NaI(Tl) detectors coupled with PC cards (Tennelec PCAP model and 93xx model, installed on PC ISA port) as multichannel analyzers. For accomplishing gamma analytical tasks, Assayer respectively Gamma2000 as Windows based MCA softwares were used.

For rapid calculations, we developed a relatively short program written entirely in Java (J2SE - free released by Sun Microsystems Inc.).

Finally, a comparison of quantitative analysis using this alternative method and the two softwares, above mentioned, has been made.

***Keywords**:* gamma spectrometry, Assayer software, Gamma2000 software, efficiency calibration

INTRODUCTION

In many specific laboratories, the NaI gamma detectors coupled with PC cards as MCA (multichannel analyzers) for data acquisition are used [1-4]. Two Windows based softwares, Assayer (distributed by Canberra Company with Tennelec PCAP PC card model, for instance) and Gamma2000 (distributed by Silena Company with 93xx PC card model, for instance) are frequently used for accomplishing gamma analytical tasks. Both softwares present advantages and disadvantages for solving several tasks as follows:

a) *Peak search and peak identify functions*:

For automatic peak search, these softwares generally use a peak finding algorithm based on convolving the spectrum with one of several "filters". The most commonly used filters are: 1) second derivate (for both softwares), 2) variable width top hat (Assayer), 3) gaussian filter (Gamma2000) [5,6]. Then, a region of interest (ROI) over the peak is created. To get the net area of the selected ROI from the raw data, a continuum correction (continuum background correction) is made

by calculating a straight-line subtraction of the continuum spectrum in the neighborhood of the peak [5]. For these tasks to be properly performed, the softwares let the user to adjust several parameters such as: the statistical test for choosing the manner which the peak is regarded to be significant, the search mode, based on filters above mentioned, and the number of channels on each side of the peak in order to perform the continuum background correction. Generally, these softwares perform the peak search and the ROI data calculations very well, but in some cases, such as the case of the spectrum with many peaks and multiplets, especially the Gamma2000 software does not properly solve these tasks. Therefore, in these cases, it is recommended to execute a manual setting of the ROIs for further calculations.

For identification of the peaks, both softwares use a multi-pass correlation technique to determine what isotope (from the user-selected library) each line is most likely to represent [5,6]. First of all, it is necessary to edit an appropriate library and also a good energy and resolution calibration is required for good identifications. An adjustable parameter is the energy window, within two lines are considered to be matched. Unlike Gamma2000, the Assayer software lets the possibility to execute a manual setting of the desired isotope for each line of the spectrum.

b) *Amplifier*:

Assayer provides the coarse gain control (brute adjustment of the bias voltage) and the fine gain control (fine adjustment of the bias voltage) to produce an overall amplifier gain, so it was possible to enlarge the energy range by decreasing the voltage until the maximum energy value was about 3000 keV. Thus, the frequently measurement of 232Th by its daughter 208Tl, which present an energy line of 2614 keV, can be done. The fine gain control can be used for adjustment in the case of the system instability that implies the slight displacement of the known peaks (e. g. calibration source).

Generally, Gamma2000 has three data acquisition modes available: *internal amplifier*, *silena probe* and *external amplifier* [2]. In this study, only the "silena probe" mode is available. In this mode, only the fine gain adjustment could be performed, thus the maximum energy value was about 2400 keV, which is insufficient for 232Th determinations.

c) *Ambient background subtraction*:

Assayer performs this correction as follows: A channel by channel subtraction is done of the ambient background spectrum (previously measured spectrum - when no sample is in detector) from the sample spectrum [5]. For good statistics, the ambient background spectrum should be measured on appropriate acquisition "live time" (unlike the real time, the live time takes into account the detector's dead time). This algorithm is not quite good because the continuum regions are also subtracted.

Gamma2000 provides a superior algorithm: first, the peak search and the ROIs setting are performed (manual adjustment is allowed) and then, the calculations of the net areas are made by continuum background corrections, both for the background spectrum and the sample spectrum. With a preset energy window (e. g. 20 keV), within energy lines are considered to be overlapped, the subtraction of these corresponding net areas is made [6]. This correction can be used in quantitative analysis but it is not allowed for the efficiency calibration calculations although, unlike Assayer, the self-absorbtion correction can be performed in both cases. If we suppose that the radioactive source used in calibration is significant strong compared with the ambient background, then the ambient background correction can be neglected.

d) *Efficiency calibration*:

Assayer works with a complex efficiency function, which has two main terms. The first term relies on the type and the physical properties of the detector (in fact, it also contains several terms). This term contains several constants and variables, which are not shown in the efficiency calibration software report. Thus, it is difficult to use the report generated efficiency equation for software independent calculations. The second term is the polynomial function of energy. The corresponding polynomial coefficients, calculated from the fitted curve, are shown in the efficiency calibration report. The least square fit on the plotted energy-efficiency pairs is previously made. The user can eliminate the unsuitable peaks, therefore an appropriate efficiency calibration can be performed.

Gamma2000 provides a good algorithm for the efficiency calibration: The user can choose either the spline interpolation method for fitting curve, which work very well for Ge detectors, or the polynomial interpolation method, recommended for the NaI systems [6]. In this last case the fit is based on two polynomes, which are used below and above the crossover energy (the energy of the junction between these two calibration polynomes). On both energy range, the least square fit is performed and the final report presents the polynomial coefficients for both efficiency equations (Ln(eff)=f(Ln(E)). These equations completely describe the energy dependencies of efficiency and can be used for independent software calculations. The user can not choose the value of crossover energy, and also the selection of the polynomial order is not allowed. Thus, the adjustment is limited only to the possibility of the peak elimination.

e) *Final activity calculations*:

Both softwares perform calculations of the activity for each peak. If the spectrum contains two or more peaks that describe the same isotope, then a final weighted average activity is computed. When the spectrum presents a peak, which corresponds to the multiple isotope lines (multiplets), the Assayer software computes an average weighted efficiency and takes into account the sum of the theoretical intensities of the spectral lines for peak activity determination [5].

In some cases, both softwares raise illegal exceptions and the applications are terminated. Sometimes, the users of Assayer software can find unexpected difficulties in editing the appropriate activity date for the efficiency calibration protocol and in editing the preset live time or in saving the tools setup parameters. When the efficiency at a high energy (e. g. 2600 keV) is small, such as a value of 0. 6%, the Assayer software can not computes the activity and a “division by null” exception is raised (the efficiency is considered to be null).

In the following section, we present an alternative software independent method for gamma analysis based on acquisition data obtained from Assayer software report.

SOFTWARE INDEPENDENT METHOD:

The calibration of the gamma system was performed by spectrum analysis of a low activity 152Eu source in water equivalent volume geometry (433 Bq +/- 5% on the measurement date). The acquisition time for source and background was 2 hours respectively 19 hours. In the case of NaI(Tl) detectors, the efficiency calibrations are not very rigorously because of: 1) statistical errors due to the fact that we used a low activity source, 2) in comparison with the Ge detectors, the NaI detectors imply significant high values of the resolution, which affect the shape of the spectrum (also, the Compton effect is strong and the multiplets appear as a large glob), thus the further gamma analysis are affected. The quantitative analysis was executed on the calibration source spectrum itself, therefore the self-absorbtion correction was indirectly considered.

The method, which will be described in this paragraph, is based on data acquisition using gamma system with Assayer software. In this case, a relatively large energy range is used for further 232Th determinations. The obtained energy and resolution calibration data are presented below (Table1 and Fig. 1-2):

The fitting curves were obtained by applying the least square method and the results are comparable with those derived from Assayer software calibrations. The last two values, from table 1, was considered for high energy evaluations. The obtained resolution of 7. 17% (full width at half maximum of the peak, FWHM = 47. 44keV) at the energy of 661. 62 keV is quite good, taking into account that the active diameter of the gama detector, used here, is relatively large (5. 5 cm).

The next step, was the ambient background analysis using the previously described Gamma2000 algorithm. Two peaks, which coresponding energies of 36. 29 keV respectively 1404. 65 keV, were considered to be appropriate in order to perform the ambient background subtraction. To apply this correction, we propose the following expression (the peaks must satisfy it, otherwise no ambient correction is made):

$$\Delta E < k * (FWHM1 + FWHM2); k = 1/4 \text{ where:} \quad (1)$$

ΔE is the energy difference of the coresponding energy lines from the sample spectrum and the background spectrum, *FWHM1* and *FWHM2* are expressions of the ROI resolutions.

Table 1.

Energy and resolution data obtained from 152Eu calibration

Center (ch)	**Energy (keV)**	**Energy (keV) from calib.**	**Error (%)**	**FWHM (keV)**	**FWHM (keV) from calib.**	**Error (%)**
21. 3	41. 01	36. 29	11. 50	12. 04	12. 46	-3. 52
41. 7	82. 01	83. 63	-1. 98	14. 94	15. 28	-2. 27
57. 6	121. 78	121. 17	0. 50	16. 09	17. 49	-8. 69
77. 8	162. 79	169. 66	-4. 22	18. 84	20. 31	-7. 82
107. 5	244. 7	242. 58	0. 87	27. 43	24. 50	10. 68
147. 5	344. 28	343. 85	0. 12	33. 42	30. 19	9. 66
304. 7	778. 9	775. 97	0. 38	49. 77	52. 86	-6. 21
366. 5	964. 13	960. 73	0. 35	57. 51	61. 76	-7. 38
411. 5	1101. 04	1100. 55	0. 04	74. 84	68. 17	8. 91
504. 8	1408. 01	1404. 65	0. 24	80. 75	81. 17	-0. 53
650		1916. 00			100. 12	
850		2696. 28			121. 98	

The efficiency calibration was performed using the Gamma2000 algorithm and taking into account of the ambient background correction. From the real peaks, we evaluated the corresponding efficiencies using the general expression:

$$eff\,(\%) = 100\,\frac{N/t - Nf/tf}{AY} \tag{2}$$

where:

N, *Nf* are the Assayer generated net counts corresponding to the source ROI respectively the background ROI,

t, *tf* are the data acquisition live time for both spectra,

A is the activity of 152Eu source at measurement date,

Y is the energy line intensity where efficiency is calculated.

The efficiency error was calculated by taking into account the net area error and the source activity error, based on the general expression (without correlation):

$$\mathrm{Sc}^2 = \sum_{i=1}^{N}\left(\frac{\partial f}{\partial x_i}\right)^2 S(x_i)^2 \tag{3}$$

where:

Sc is the composed error; in our case it represents the efficiency error,

f is the function ; in our case represent the efficiency expression (eq. 2),

xi are the variables having *S(xi)* as uncertainties . In our case *N*, *Nf* and *A* with corresponding errors are involved.

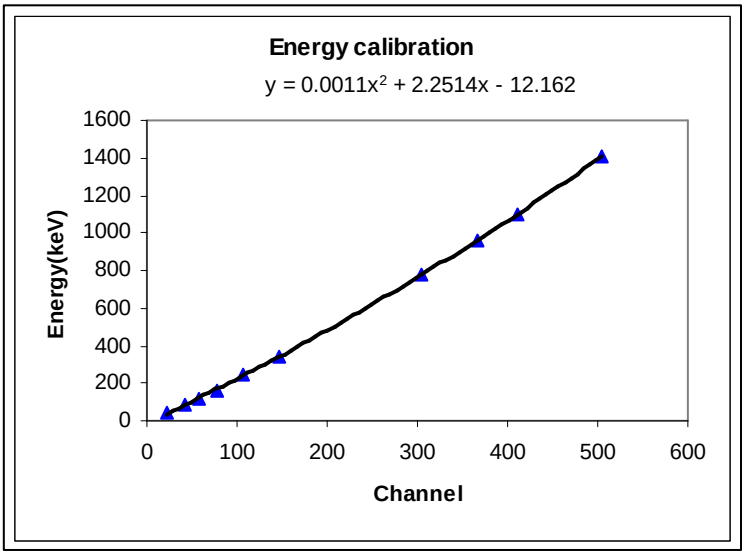

Fig. 1. Energy calibration

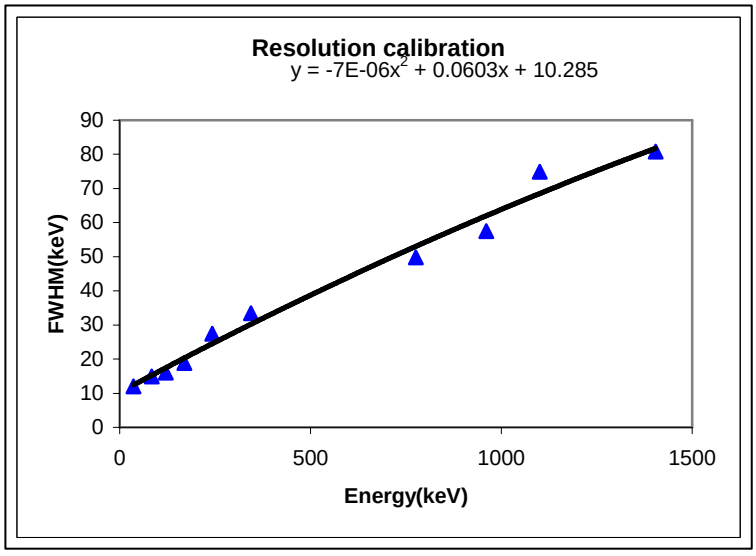

Fig. 2. -Resolution calibration

With these considerations, we obtained the values from Table 2:

Table 2. Efficiency determination and associated uncertainties

Channel (center)	Energy(E) (keV)	Efficiency (%)	Error	Overall error(%)	Efficiency (%) From calib.	Fit error (%)
21. 31	36. 31	8. 43	0. 02	2. 91	8. 43	0. 00
57. 57	121. 10	7. 80	0. 05		7. 80	0. 00
107. 71	243. 10	5. 04	0. 16		6. 87	-36. 22
147. 65	344. 24	5. 24	0. 06		5. 24	-0. 06
304. 85	776. 40	2. 04	0. 09		1. 92	5. 76
366. 50	960. 73	1. 14	0. 08		1. 51	-32. 97
410. 98	1098. 91	1. 64	0. 05		1. 33	19. 19
504. 73	1404. 41	1. 04	0. 04		1. 09	-5. 21

If, E_c is the crossover energy, two polynomes, as function of energy, having *n* respectively *m* order, were choosen on (0-E_c) respectively (E_c-maximum energy value) energy range:

$$f(E)= a_0+a_1Ln(E)+\ldots+a_nLn(E)^n,\ E<Ec \quad (4a)$$

$$f(E)= b_0+b_1Ln(E)+\ldots+b_mLn(E)^m,\ E>Ec \text{ where} \quad (4b)$$

$a_0,\ldots a_n,b_0,\ldots b_m$ are the polynomial coefficients which will be estimated.

Generally, if x_i and y_i are the pair values for the plotted function, $f(x_i)$ is the proposed analytical function, the least square fit method requires that the follow expression to be minimized:

$$S=\sum_i [y_i - f(x_i)]^2 = \min \quad (5)$$

In our case x_i is Ln(E_i) and y_i is efficiency (%) at energy E_i. Similarly, x_c is Ln(E_c) and y_c represent efficiency (%) at the crossover energy.

Let p_1 and p_2, the number of energy-efficiency pairs on both sides of the crossover energy.

With these considerations, we computed the following expressions:

$$\partial S/\partial a_i=0,\ \partial S/\partial b_i=0 \quad (6)$$

Taking into account the continuity equation at crossover energy, we obtain the following equation system (n+m+3 variables with n+m+3 equations):

$$a_0[\sum_{i=1}^{p_1} 1+1]+a_1[\sum_{i=1}^{p_1} x_i+x_c]+\ldots+ a_n[\sum_{i=1}^{p_1} x_i^n+x_c^n]= \sum_{i=1}^{p_1} y_i+y_c$$

$$a_0[\sum_{i=1}^{p_1} x_i+x_c]+a_1[\sum_{i=1}^{p_1} x_i^2+x_c^2]+\ldots. +a_n[\sum_{i=1}^{p_1} x_i^{n+1}+x_c^{n+1}]=\sum_{i=1}^{p_1} x_iy_i+y_cx_c \quad (7)$$

$$a_0[\sum_{i=1}^{p_1} x_i^n+x_c^n]+a_1[\sum_{i=1}^{p_1} x_i^{n+1}+x_c^{n+1}]+\ldots. +a_n[\sum_{i=1}^{p_1} x_i^{n+n}+x_c^{n+n}]=\sum_{i=1}^{p_1} x_i^n y_i+y_c x_c^n$$

$$b_0[\sum_{i=1}^{p_2} 1+1]+b_1[\sum_{i=1}^{p_2} x_i+x_c]+\ldots+ b_m[\sum_{i=1}^{p_2} x_i^m+x_c^m]=\sum_{i=1}^{p_2} y_i+y_c$$

$$b_0[\sum_{i=1}^{p_2} x_i+x_c]+b_1[\sum_{i=1}^{p_2} x_i^2+x_c^2]+\ldots. +b_m[\sum_{i=1}^{p_2} x_i^{m+1}+x_c^{m+1}]=\sum_{i=1}^{p_2} x_i y_i+y_c x_c$$

……

$$b_0[\sum_{i=1}^{p_2} x_i^m+x_c^m]+b_1[\sum_{i=1}^{p_2} x_i^{m+1}+x_c^{m+1}]+\ldots. +b_m[\sum_{i=1}^{p_2} x_i^{m+m}+x_c^{m+m}]=\sum_{i=1}^{p_2} x_i^m y_i+y_c x_c^m$$

$$a_0+a_1x_c+\ldots+a_nx_c^n=b_0+b_1x_c+\ldots+b_mx_c^m$$

To properly solve this equation system and to easily change E_c, p_1 and p_2 in order to obtain a good efficiency calibration, we developed a relatively short Java program (J2SE- free released by Sun Microsystems Inc.). This program, read the input energy-efficiency pairs, E_c, p_1 and p_2, put the system in matrix form and then solve it, using the Gauss elimination method for linear equation systems [7]. We did not consider the efficiency at 243. 10 keV because it is less then the efficiency at 344. 24 keV due to the measurement errors of the NaI system. The following results (Table3 and Fig. 3) are for the case that the crossover energy has a value of 300 keV and the both polynomial order have a value of 3, in order to provide the best fit.
The general form of efficiency function, used here, is:

$$eff(\%)=f(Ln(E)) \quad (8)$$

Table 3. Equations coefficients and crossover values for efficiency calculations

coeff.	**1st polynome Java calc.**	**2nd polynome Java calc.**	**Crossover (keV)**	**eff. (crossover) (%)**
c_0	81. 53578509	262. 7532264	300	6. 17
c_1	-49. 50207102	-101. 1794431		
c_2	11. 0967569	13. 0780933		
c_3	-0. 830078125	-0. 565584396		

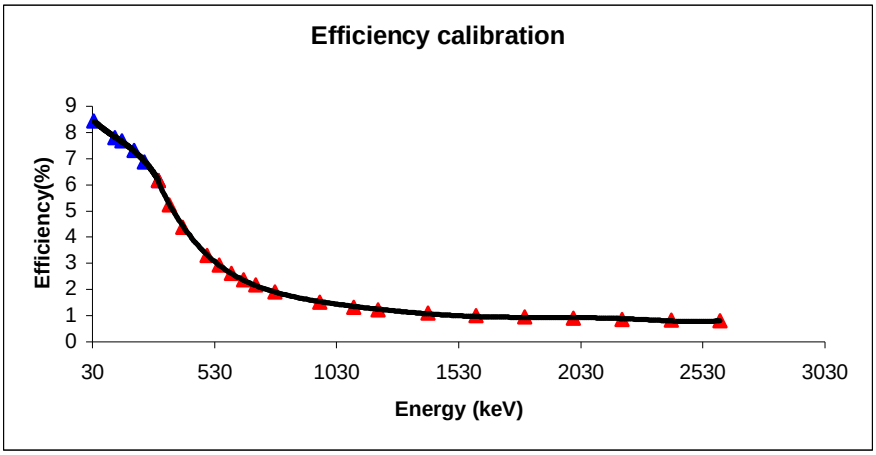

Fig. 3. –Efficiency calibration

The average fit error was 12. 42% and the efficiency computed from the fitted curve at the energy value of 344. 24 keV was 5. 24% (table 2). At 2600 keV, efficiency has a value of 0. 8%, so it is possible to compute the 232Th activity by 208Tl determination in further calculations (the self-absortion at this energy can be neglected). We also mention that we was interested to obtain good results, including the shape of the curve, only for energies higher then 100 keV because the low energy determinations are not performed using the NaI(Tl) detectors. Using the same source (152Eu) and a 75X75mm NaI(Tl) detector coupled with a four channel gamma analyser (NY-424-Hungary) an efficiency of 6. 5 % was determined for 344 keV energy [8]. In our case, 55X55mm detector, the founded value was 5. 24 % (see Table 2 and Fig. 3)

For minimum detectable activity (MDA) estimation on each ROI, we consider the Assayer algorithm as model. Based on the Poisson statistics, which is specific to the nuclear desintegrations, this model assumes the following equation for MDA [5]:

$$MDA=(2.71+4.65)\sqrt{K}/(t\cdot Y\cdot eff) \text{ where:} \quad (9)$$

K is the continuum background count,

t is the sample spectrum live time,

Y is the line intensity of coresponding energy,

eff is the efficiency at the coresponding energy.

The MDA error is evaluated based on the general expression (eq. 3) where, as variables, we have the efficiency error and the continuum background error.

All errors involved in the final results are given with a 95% confidence level.

We also used the Assayer algorithm to estimate the final activity. If w_i is the weighted factor defined as:

$w_i = A_i/S_i$ where (10)

Ai is the activity computed from spectrum line i,

S_i is the uncertainty associated to A_i,

the final activity is:

$$A = \frac{\sum_i w_i A_i}{\sum_i w_i}$$, with uncertainty: (11)

$$S = \frac{\sum_i w_i^2 S_i^2}{[\sum_i w_i]^2}$$ (12)

The 152Eu source presents an activity of **433Bq+/-5%** at the measurement date. Obviously, the activity value computed from each peak is statisticaly greater then the corresponding MDA.

The computed activity at the reference peak of 344. 28keV and the final activity, evaluated using the above mentioned algorithms, are as follows (Table 4):

Table 4. Activity calculations for 152Eu source

Method	Activity at 344. 28 keV	Final activity
This method	432. 27 +/- 9. 16 Bq	435. 65 +/- 9. 31 Bq
Assayer	426. 90 +/- 22. 80 Bq	429. 00 +/- 14. 16 Bq
Gamma 2000	525. 14 +/- 5. 98 Bq	429. 77 +/- 121. 95 Bq

CONCLUSIONS

These softwares, present advantages and disadvantages and we developed an alternative method based on the best algorithms of Assayer and Gamma2000, for accomplishing the gamma spectrometry tasks.

Sometimes, a manual setting of ROIs is the best choice that user could have, in order to perform further good analysis.

The ambient background subtraction is properly performed by Gamma2000, but this correction is not allowed on efficiency calibration routine.

With all these methods, it was obtained good results for the final activity, but for the activity determination at a reference peak of 344. 28 keV, only this method and the Assayer one provide appropriate results.

Using Gamma2000, in conditions presented above, it is impossible to evaluate the 232Th activity by its daughter 208Tl at 2600 keV (the best solution for NaI systems). Using Assayer, we can perform only soft independent calculations

for this kind of determinations. These 232Th determinations are frequently performed in our laboratories.

The errors involved in final Gamma2000 calculations are relatively big, due to the fact that the all peak interferences was considered [6]. Therefore, a better isotopic library configuration is required.

Performing manual calculations, based on the Assayer software generated report, which present the acquisition data including the efficiency values, we found some errors in the Assayer calculations, especialy for the uncertainty estimation of the peak activity.

Finaly, to evaluate the final activity from only one peak, the software independent method, which is presented in this paper, provide the best result.

REFERENCES

1. I. C. Yang, E. Abbats, Gamma-Emitting Radionuclide Measurements at the U. S. Geological Survey National Water, Nucl. Instrum. Meth,193,197-211,(1982)
2. O. Sima, Health Physics, 62, 445-449, (1992)
3. C. Cosma, L. Daraban et al., Czech. J. Physics,49,213-216 (1999)
4. I. Chereji et al., J. Radioanal. Nucl. Chem., Lett., 212,85-92,(1995)
5. American Nuclear Systems, Inc., Quantum Assayer-Quantitative Analysis for Nuclear Spectroscopy, 1993-1997, USA
6. Silena International S. p. A., Gamma2000 Application Software package-Instruction manual rev. 2. 0, 2000, Italy
7. T. Beu, Numerical Analysis in Turbo Pascal, Ed. Microinformatica,Cluj-Napoca,1993
8. C. Cosma, (to be published)

STUDIA UNIVERSITATIS BABEŞ BOLYAI, PHYSICA, L, 1, 2005

STRUCTURAL CHANGES INDUCED BY SIMULATED BODY FLUID ON SURFACE OF SINTERED TITANIUM-HYDROXYAPATITE IMPLANT MATERIALS

S. SIMON[1*], D. MURESAN[1], C. POPA[2], I. BALASZ[1], V. SIMON[1]

**Corresponding author: simons@phys.ubbcluj.ro*
[1]Babes-Bolyai University, Faculty of Physics, Cluj-Napoca,Romania
[2] Technical University of Cluj-Napoca,
Faculty of Materials Science and Engineering, Cluj-Napoca,Romania

ABSTRACT. Hydroxyapatite (HA) coating is the common approach to improve the biocompatibility of orthopaedic and dental titanium-based implants. Biologically active HA being similar to the mineralised bone tissue may be developed under *in vivo* simulated conditions. An important aspect is the ability to nucleate HA type crystals from a simulated body fluid. The effect on the bioactive phase developed on the surface of titanium-hydroxyapatite samples was evidenced by microscopic analyse after soaking for seven days in simulated body fluid. These materials are promising for developing hard tissue implants with good mechanical properties and high bioactivity.

Introduction

Functionally graded materials (FGM) consisting of metallic and ceramic components [1] are well known to improve the properties of several systems such as medical implant devices. Hydroxyapatite is known to be both biocompatible and bioactive material, however, due to its poor mechanical properties and design limitations is not suitable for applying as a load bearing implant. This could be overcome by using appropriate metallic enforcer with hydroxyapatite [2-4]. Titanium implants have a thin oxide surface layer, which may explain their good biocompatibility [5]. These solutions allow improved adhesion strength of the load bearing metallic component to the bone, resulting in shorter healing periods as well as predictable behaviour of the implant for longer periods of time. There are different techniques of producing HA appropriate for these purposes. Sol-gel technology offers an alternative technique for producing bioactive surfaces for improved bone attachment. Ti-HA sintered powders shown to induce HA formation upon exposing to simulated body fluid [6-8]. In the last time sol-gel method is conventionally used to obtain HA powder or thin film coating [9, 10].

This paper deals with a new class of active FGM including sintered titanium with hydroxyapatite that can ensure a bioactive surface phase. The focus is on the characterization of the structure of the graded layer before and after immersion in a simulated body fluid as the development of an active layer is expected.

EXPERIMENTAL

Titanium powder (0.01%Fe; 0.01%Al; 0.001%Si; 0.05%Mg) with the grain size of 63 - 100 μm was used. The powder was obtained through the hydrating – milling – dehydrating process and the grains display a specific shape. Hydroxyapatite was obtained through a sol-gel technique, burnt and milled to obtain a powder with the grain size of less than 40 μm. Samples with 5 weight % hydroxyapatite were mixed in a tubular mixer. Powders were pressed by applying a forces of 30 kN in a rigid die with the surface of 0.5 cm^2, without the use of any lubricant. The compacts were subsequently vacuum sintered (10^{-6} torr) at 1160°C for 60 minutes, with dwelling stages at 200, 600 and 800°C.

The phase of hydroxyapatite type was prepared by sol-gel method. The precursor reagents were calcium nitrate $Ca(NO_3)_2$ as a source of calcium ions and ammonium phosphate $(NH_4)_2HPO_4$ as the phosphorus precursors. The molar ratio of precursors Ca/P was 1.67. The distilled water solution of phosphorus precursor was added to the calcium nitrate solution heated at 90^{o}C. After mixing the sol-gel was washed at room temperature and dried for 2 hrs at 110^{o}C. The dried sol-gels were heat treated in air for 3 hours at 900°C and for 1 hour at 1150 °C.

X-ray diffraction analysis (DRX) was carried out on powder and sintered samples using a Bruker Avance diffractometer. The bulk density of the samples was determined using Archimedes method. Bioactivity was investigated by an in-vitro test. The samples were soaked in simulated body fluid (SBF) solution. Exposure experiments in SBF of pH 7.4 [11] were conducted at 37 °C in polystyrene vials. The surfaces were characterized by optical microscopy. The microstructure on randomly selected areas was observed with a stereo optical microscope Nikon Eclipse E200 equipped with CCD camera Nikon Kooply X995.

RESULTS AND DISCUSSION

The density often inferred as bone mineral density is expected around 2.982 g/cm^3 [12]. The density of bulk pure titanium is 4.507 g/cm^3. To overcome this additional disadvantage many attempts have been done to reduce the density and to induce the bioactivity of titanium implant materials by sintering metallic titanium powder and bioactive inorganic filler. The bulk density of Ti-HA studied samples is encompassed between 3.05 and 3.08 g/cm^3. These values are very convenient for orthopaedic biomaterials.

X-ray diffraction patterns (Fig. 1) of the sol-gel hydroxyapatite type powder show in the as prepared sample a large structural disorder degree and the occurrence of relatively large peaks corresponding to crystalline calcium phosphate (marked with ▪ in Fig. 1a-c), while the applied heat treatments induce the crystallisation of several apatite type crystals (marked with ◆ in Fig. 1b and 1c).

The surface of the sintered samples was characterized by optical microscopy. Homogeneous mixtures of the two phases entering these functionally graded materials are evidenced, as can be seen in Figure 2a. Due to the fact that from XRD patterns (Fig.

3a) only α-titanium lines of metallic phase [13] have been identified one can assume that the second phase consists of vitreous calcium phosphate or very distorted crystals. The titanium metallic phase seems to be form by crystals preferentially oriented to the sample surface. These effects on the both phases are due to the relatively high sintering temperature (1160^{o}C) and high pressure used for samples processing.

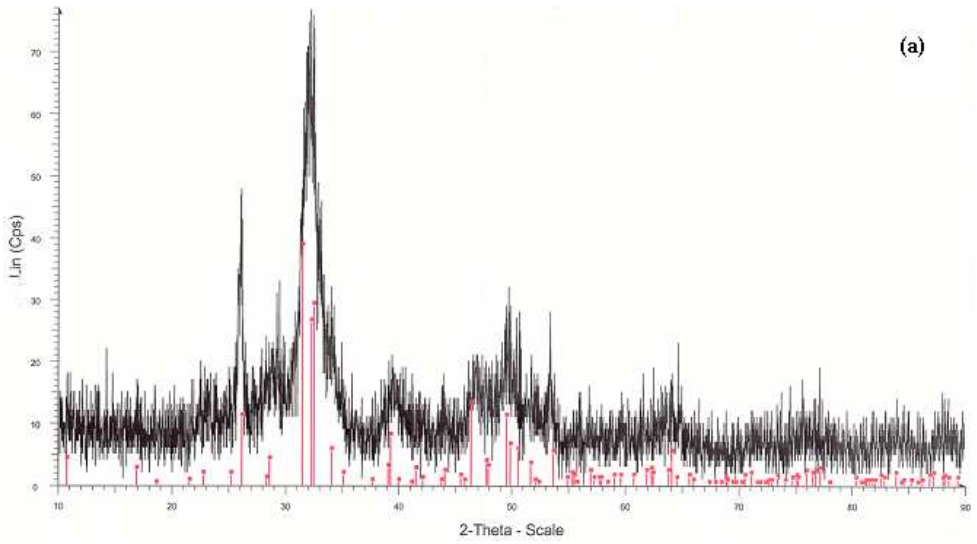

Fig. 1. DRX patterns of the **(a)** as prepared sol-gel sample

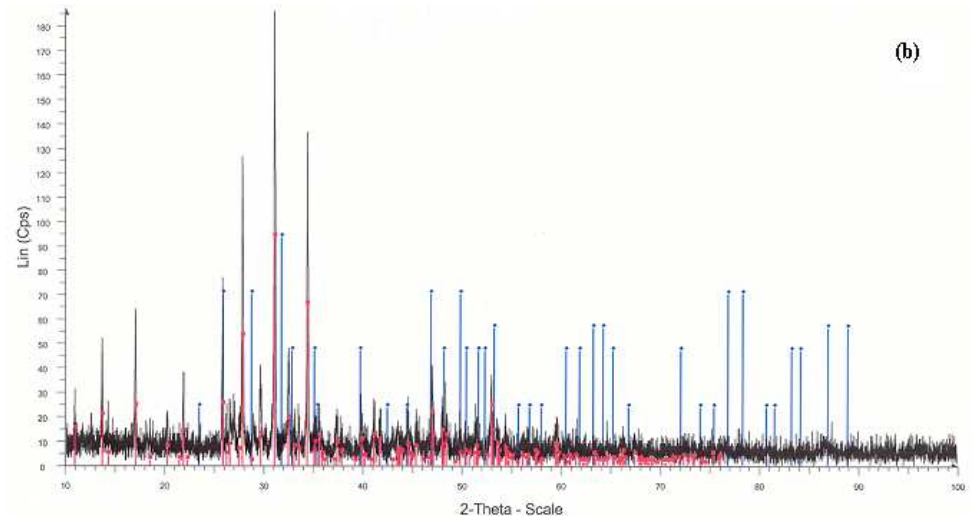

Fig. 1. DRX patterns of the **(b)** sol-gel sample heat treated at 900^{o}C and

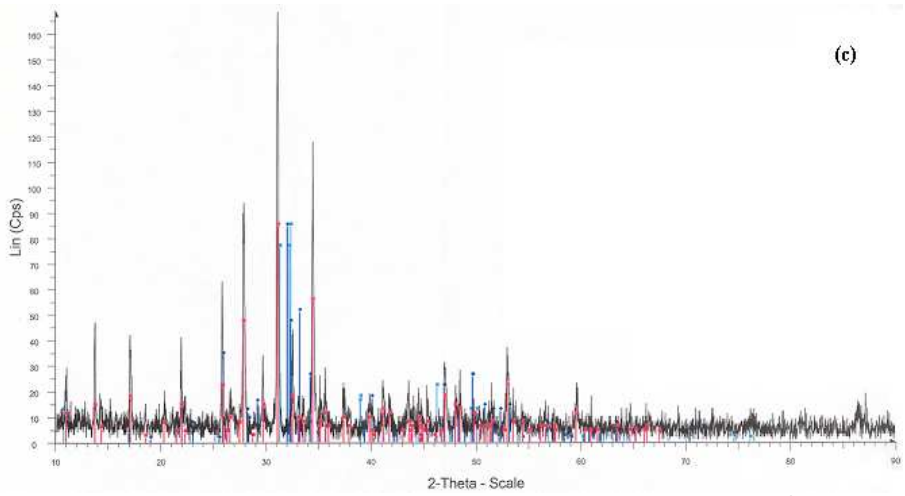

Fig. 1. DRX patterns of the **(c)** sol-gel sample heat treated at 1150^{o}C.

An essential requirement for an artificial material to bond to living bone is the formation of a biologically active HA-like layer on its surface in a body environment [14]. Therefore these materials are also called biomimetic systems [15, 16]. Metallic implants are often coated with a layer of a bioactive material to improve bone-bonding ability [17].

In order to check the bioactivity the samples were soaked for 7 days in SBF (pH = 7.4) and maintained between 37 and 40^{o}C. The SBF contains certain proportions [11] of NaCl, $NaHCO_3$, KCl, $K_2HPO_4 \cdot 3H_2O$, $MgCl2 \cdot 6H_2O$, 1N-HCl, $CaCl_2$, Na_2SO_4 and $NH_2C(CH_2OH)_3$ (trishydroxymethylaminomethane- as buffer). The ratio between SBF volume to sample surface area was around 30 m. At the surface of the samples immersed in SBF one can observe after 7 days an expansion of calcium phosphate phase (Fig. 2b). The microtexture of the surface is dominated by HA type phase. On immersion in SBF, one observes that the bioactive phase is extended at the expense of titanium phase. These HA type polycrystalline phases developed at the surface of Ti-HA powder sintered samples after seven days immersion in SBF have the size up to 0.35 mm and are confirmed in XRD pattern (Fig. 3b) by appearance of new intense lines at $2\theta = 29.5^{o}$ and 35^{o}. An other effect of the SBF soaking is observed on the titanium microcrystals orientation on the sample surface, that are after seven days immersion in SBF randomly oriented.

At the same time one remarks the tendency to form a continuous network of the new developed bioactive layer formed in interaction with the SBF as result of interface interactions and cations exchange, primary with the HA type phase.

The formation of the bioactive phase could be also induced by the Ti-OH groups, which reveals negative charge to interact with calcium ions in the SBF. The amorphous calcium titanate is postulated to reveal positive charge, thereby interacting with the phosphate ions in the fluid to form the amorphous calcium phosphate, which eventually crystallized into HA-like phase [18].

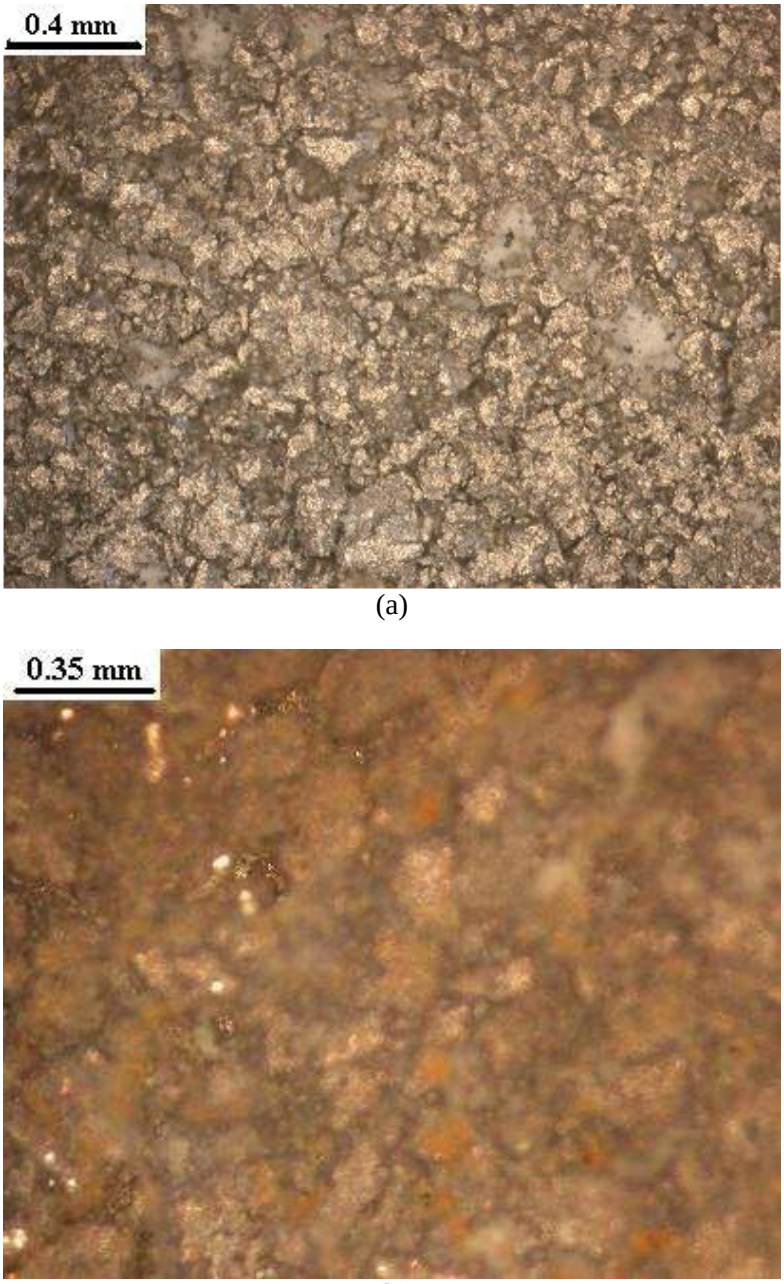

(a)

(b)

Fig. 2. Optical microscopies from sintered 95Ti-5HA samples (a) before and (b) and after soaking in SBF.

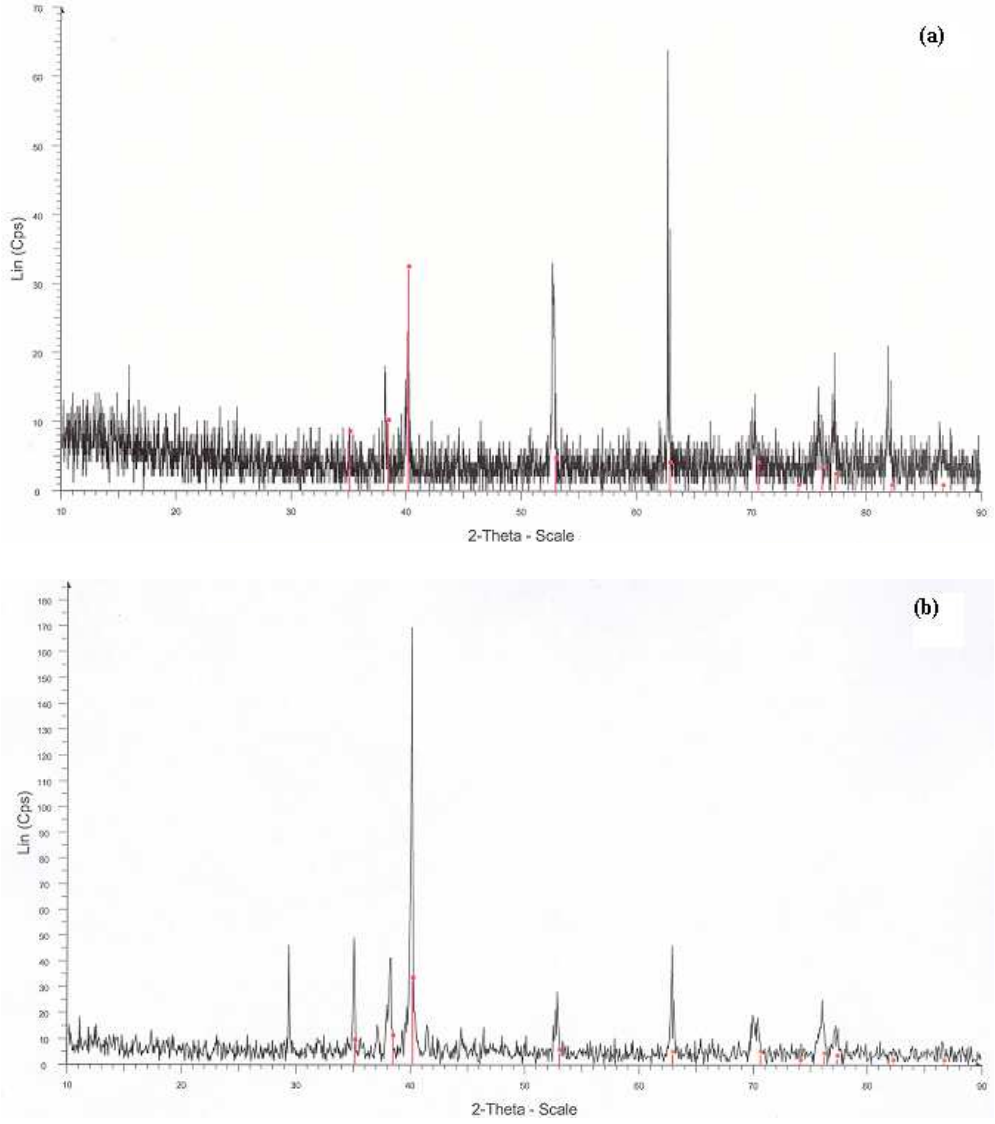

Fig. 3. DRX patterns of the 95Ti-5HA samples (a) before and (b) after soaking in SBF.

CONCLUSIONS

Sintered powder Ti-HA samples were obtained as a new bioactive FGM class. Their density is very convenient for bone implant materials. In vitro these materials proved to have bioactive behaviour. The size of HA type phases developed at the sample surface after soaking for a week in SBF is about hundreds of micrometers

and trend to form a continuous network of the new developed bioactive layer. At the same time the titanium metallic grains, as result of the interface processes, are randomly oriented.

REFERENCES

1. J. Aboudi, M.-J. Pindera, S.M. Arnold, J. Appl. Mech., 68, 5 (2001) 697
2. T. Miyazaki, H.M. Kim, F. Miyaji, T. Kokubo, T. Nakamura, Bioceramics 10, Elsevier Science LTD, 1997
3. H.M. Kim, F. Miyaji, T. Kokubo, T. Nakamura, J. Ceram. Soc. Jpn. 105, 2 (1997) 111
4. D.A. Cortes, J.C. Escobedo, A. Nogiwa, A. Mu?oz: Mater. Sci. Forum, 442 (2003) 61
5. Y. T. Sul, C. B. Johansson, Y. Jeong, T. Albrektsson, Medical Engineering & Physics, 23 (2001) 329
6. H.M. Kim, F. Miyaji, T. Kokubo, T. Nakamura, J. Biomed. Mater. Res. 32 (1996) 409
7. H.M. Kim, F. Miyaji, T. Kokubo, S. Nishiguchi, T. Nakamura, J. Biomed. Mater. Res. 45 (1999) 100
8. H.B. Wen, J.R. de Wijn, F.Z. Cui, K. de Groot, Biomaterials 19 (1998) 215
9. D.M. Liu, T. Troczynski, W. J. Tseng, Biomaterials, 22 (2001) 1721
10. V. Simon, D. Muresan, C. Popa, S. Simon, Int. Conf. on Biomaterials BiomMedD'2004, Bucharest, 5-7 Nov. 2004
11. T. Kokubo, S. Ito, Z.T. Huang. T. Hayashi, S. Sakka, T. Kitsugi, T. Yamamuro, J. Biomed. Mater. Res., 24 (1990) 331
12. E.M. Evans, B.M. Prior, S.A. Arngrimsson, C.M. Modlesky K.J. Cureton, J. Appl. Physiol., 91, 5 (2001) 2166
13. R. Sailer, G. McCarthy, JCPDS 44-1294, Int. Centre for Diffraction Data (1993)
14. T. Kokubo, H.-M. Kim and M. Kawashita, Biomaterials, 24 (2003) 2161
15. Y. Abe, T. Kokubo and T. Yamamuro: J. Mater. Sci.: Mater. Med., 1 (1990) 233
16. J.F. Shackelford: Mater. Sci. Forum, 293 (1999) 99
17. L.L. Hench, Mater. Sci. Forum, 293 (1999) 37
18. H.M. Kim, H.Kaneko, M. Kawashita, T.Kokubo, T.Nakamura, Key Eng. Mat., Bioceramics 16, 254-256 (2004) 741.

STUDIA UNIVERSITATIS BABEŞ BOLYAI, PHYSICA, L, 1, 2005

RADIUM-226 MEASUREMENTS FROM UNDERGROUND WATERS IN DEJ AREA

M. MOLDOVAN[1], C. COSMA[2], D. RISTOIU[2]

[1]"Babes-Bolyai" Univesity, Faculty of Physics, M.Kogalniceanu, 400084 Cluj-Napoca, Romania
[2]"Babes-Bolyai" University, Faculty of Environmental Science, Cluj-Napoca

ABSTRACT. The most important radionuclids from water and gas radioactivity point of view are: the uranium, the radium and the radon with it's short life descendents.

This paperwork determinate the radium concentration from underground and surfaces waters in Dej area comparatively with others Romanian regions. We used Luk-3A Czech device. Using this device we can determine the radium concentration indirectly, after we measure the radon resulted from balanced radium-226. The direct forerunner of radon is secular balanced with the radon-222.

The 25 samples were taken from Dej area. After the measurements we obtained a 3.7 pCi/ average (the minimum value was 0.61pCi/l and the maximum value 10,47 pCi/l).

This radium measurements are important because the sources for the water that we drink are the underground waters, so we can foresee an possible contamination which concerns the population.

Introduction

The risc of radium exposure and the radiation effects on living tissue have large perspective affinity in Physics, Medicine and Geology.

The involvement of radium and especially of radon in population iradiation lead to the conclusion that this element represents the second majour risc factor, after smoking, in pulmonary cancer.

The first phase in preventing the exposure risk at radium and radon is the identification of the sources and then finding the best way to rectify the situation.

Radium is formed by uranium and thorium desintegration in the environment. Radium desintegrates by α radioactive emmision. Due to the fact that uranium can be found throughout the terestrial crust, radium presence can be considered everywhere. It can be found in soil, watter, rocks, plants, building materials and in lower concentrations in food. There are four isotops of radium that are naturally obtained ^{226}Ra, ^{223}Ra, ^{224}Ra, ^{228}Ra and more isotops produced by man through desintegation [1].

The soil and rocks content in ^{226}Ra can be direct determined by spectrometry or by quantity analysis of ^{222}Rn which is in secular equilibrium with ^{226}Ra in solid or liquid samples.

^{224}Ra can be determined with good precision by considering the secular equilibrium with its life long parent, ^{232}Th, by α spectrometry. This last method can also be used in ^{223}Ra determination.

^{226}Ra discovered by Marie Curie was used in medical purposes and it is up-to-dateness again as the parent of radon, the last one becoming a real threat in houses and work places when its concentration is too high.

Radium in water

The concentration of ^{226}Ra and ^{228}Ra in the drinking water are usually low, but there are areas where the high concentration of radium is due to the geological sources. The surface water usually has a very low radium concentration, but the underground waters may contain higher concentrations due to the local geology. Sometimes the drinking water from wells may contain ^{226}Ra and ^{228}Ra at higher levels than the standard ones.

A research project lead by the USA Public Health Service (PHS) made a retrospective study of the homes of 111 comunities from Illinois and Iowa, which were given water containing over 3pCi/l of radium [2]. A total of almost 908.000 inhabitants was the exposed population. In another study made on the public water from these comunities showed that the averege level of Radium in water is 4,7 pCi/l. [3]

According to the PHS estimations, the maximum level of contamination for Radium (combined ^{226}Ra and ^{228}Ra) from the public water is 5 pCi/l.

The consumption of water with a 5 pCi/l Radium concentration for a year is comparable to the cosmic radiation exposure during a single transoceanic flight at approximately 15.000 km altitude.

The measuring method of the Radium-226 in water

Generally, ^{226}Ra, the direct parent of radon, is in secular equillibrium with the last one. We note with λ_{Ra} and λ_{Rn} the desintegration constants of radium, respectively radon, adn with N_{Ra} and N_{Rn} the number of atoms of radium, respectively radon. In the case of secular equilibrium, for a time $t<<T_{1/2}(Ra)$, where $T_{1/2}(Ra)=1620$ years, $T_{1/2}(Rn)=3,82$ days, the parent radium desintegration speed is actually constant :

$$N_{Rn} = N_{Ra} \frac{\lambda_{Ra}}{\lambda_{Rn}}$$

which means that the activities of the parent (^{226}Ra) and the daughter (^{222}Rn) become equal.

Experimental method

For radium determinations, we actually measure radon using a LUK-3A Czech device. The special device for radon extraction from water that accompanies the LUK 3A device is called LUK VR.

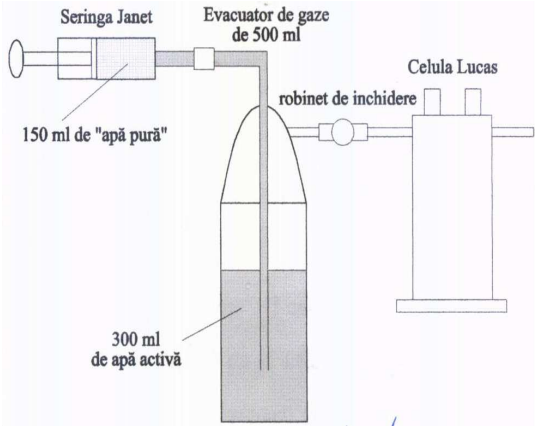

Figure 1. The principle scheme of the LUK-VR device:
- 500 ml gase evacuation
- tap with robber connectors
- termometer

The procedure used for radium measurement in water

The Radon activity concentration is equal to the radium activity concentration, this happens after a a period of 28 days when radium can be considered in secular equilibrium with radon. In all the used calculations we will refer to radon activity concentration measurement which is actually the activity concentration of radium.

The procedure can be resumed to the following steps:

a) the water sample processing:

- the water samples will be taken in 0,5 l botles, the vessels will be fully filled and perfectly closed

b) the botle will be brought to room temperature and the water temperature will be noted.

c) the water sample from the bottle, after reaching equilibrium is poured in the LUK-VR (scrubler) radon extraction device from water. After one minute of stirring, the scrubler is connected to the Lucas cell from the inside of the Luk-3A device.

d) The number of impulses given by the sample is recorded on a pre-established time interval. This number of impulses is chosen so that the statistic errors are around ±20% in our case, which means that the total number of measured impulses is around 40.

The study results

The first stage of these radium studies was carried on in Dej area and included the most important villages from this region. All samples were taken on November 2003, using the procedure mentioned above.

Cluj area has always been extremely interesting from the point of view of a study regarding the water and soil radioactivity. The hills that characterise this region of Transylvania and the variety of soil are just two of the factors that motivate the making of this study.

The first step included Dej area, with all the geographical interest points and took. The second stage of the research was made in different regions of Cluj area and in other regions of the country.

Figure 2. The places around Dej where radium was measured

Table 1. Radium concentrations values from Dej area

No	Colecting place	source	Impulses no/600s	Concentration Bq/l	Concentr. pCi/l
1	Cart Viile Dejului	Well	15.99	0.033	1.23
2	SC.Gen. nr.2	Spring	16.98	0.116	4.31
3	Apă dedurizată		16.98	0.0165	0.6105

No	Colecting place	source	Impulses no/600s	Concentration Bq/l	Concentr. pCi/l
4	Cart. Mulatău	Well	25.98	0.2165	8.016
5	Dej	Tap	12.99	0.05	1.85
6	Cart.Ocna-Dej	Well	30.99	0.15	5.55
7.	Șomcut	Well	15	0.083	3.085
8	Țibleș nr.51	Well	12.99	0.065	2.46
9	Toroc	Salted	30.99	0.285	9.48
10	Plevna nr. 11	Well	21	0.185	6.85
11	Dej	Spring	19.98	0.1	3.7
12	Sat Suia	Well	24	0.2	7.4
13	Cart. Sinistrați	Well	5.66	0.11	4.31
14	Gherla	Tap	12.99	0.016	0.61
15	Car Ocna Dej-Cupșa	Well	21.48	0.175	6.47
16	Ocna Dej 1	Well	22.98	0.21	8.02
17	Ocna Dej 2	Well	19.98	0.16	6.16
18	Ocna Dej 3	Well	15.99	0.065	2.4
19	Ocna Dej 4	Well	27.99	0.283	9.47
20	Ocna Dej 5	Well	21	0.117	6.47
21	Dej-Triaj	Well	21	0.175	6.74
22	Cuzdioara	Well	21	0.175	6.74
23	Sânmarghita	Salted	24.98	0.23	8.6
24	Sânmarghita	Well	18	0.05	1.85
25	Sânmarghita	Well	24	0.183	6.78
26	Cart. Viile Dejului	Well	21	0.117	4.32
27	Dej	Spring	22.98	0.133	4.9
28	Dej	Well	27.99	0.23	8.51
29	Valea Copandului	Well	21	0.133	4.9
30	Orman	Well	21.99	0.116	4.13
31	Țaga	Well	15.99	0.083	2.96
32	Buza	Well	16.98	0.066	2.46
33	Bonțida	Well	13.98	0.05	1.85
34	Sic	Well	18	0.067	2.47
35	Iclod	welll	26.98	0.05	1.85
	Average			0.12	4.78

The values obtained for the background are between 2.33 and 5.33 for t=200 sec., therefore, for 100 sec. we have a background between 1.165 and 2.66.

As it can be seen from Table 1 the minimum value obtained is 0.61 pCi/l, and the maximum value is 9.48 pCi/l. The averege value is 4.78 pCi/l.

The highest values of the radium concentration were obtained around Ocna Dej.

By comparison, in Table 2, are shown the radium concentrations in other regions of the country.

Table 2. Results from different regions of the country

Nr	Place	Source	Imp. no/600s	ConcentrationBq/l
1	Cluj-Napoca	Tap	21	0.15
2	Alba	Tap	27.99	0.233
3	Bistrița	River	15.99	0.1
4	Bistrița	Lake	15.99	0.067
5	Zalău	Tap	21	0.083
6	Mihai Viteazu	Lake	16.99	0.5
7	Mihai Viteazu	Spring	25.98	0.25
8	Toplița	Spring	21.99	0.15
9	Toplița	thermal	19.99	0.15
10	Zalău	Tap	18	0.0083
11	Turda	Tap	18.99	0.05
12	Râmnicu Vâlcea	Tap	18.99	0.1
	Average			0.12

From the obtained values we see a maximum value of 9,25 pCi/l in Mihai Viteazu, and the minimum value of 1,85 pCi/l was obtained in Turda from the drinking water source. The averege value is 4,6 pCi/l and is the same as in Dej area.

Conclusions

We analised radium concentaration from drinking water from Cluj region and other few areas.

The results of the study from Dej region show the following:

The radium concentration in underground water is high in the wells from Ocna Dej area. There are two values closed to the maximum value, Mihai Viteazu from Alba region, and respectively Mulatau neighbourhood Dej.

The radium concentration in water has a moderated value in the the wells from Dej area.

All the results of the studies about radium in Cluj region show that the radium concentration values measured in this region are comparable with values measured and given in literature and they are under the maximum accepted values [4]. In the ground water from a voulcanic zone in Central Mexico were found similary values, about 2.7 pCi/l as average [5].

To improve the statistic errors a measuring time for background and samples is neccesary.

REFERENCES

1. C. Cosma, T. Jurcuț, I. Pop, D. Ristoiu, *Depunerea de radiu în instalațiile geotermale din Oradea*, Analele Universității din Oradea, 5-85, 1995
2. *Speak now Regarding USEPA's Radon in Water Proposal*, Water Online News and Analysis 13 mar. 2000
3. M.A. Robkin, *Dosymetry Models*, Indoor Radon and its Hazards, Univ. of Washington Press, 1989, pag. 76-89
4. C. Cosma, T. Jurcuț, *Radonul şi mediul înconjurător*, Ed. Dacia, Cluj-Napoca, 1996
5. N. Segovia, P. Aranda, A. Hernandes Environmental Radiochemical Analysis, The Royal Societe of Chemestry, 1999, pg 37-45
6. C. Cosma, I. Pop, S. Ramboiu, T. Jurcut, *Environmental Radioactive Aspects of Geothermal Water use in Oradea*, World Geothermal Congress, Rome, 4, 1995
7. C. Cosma, A. Poffijn, D. Ristoiu, G. Messen, *Radon in Variuos Environmental Samples in Herculane Spa*, Cerna Valley, Environment International, 24, 1-4, 1996
8. A.E. Nevissi, D. Brodansky, *Radon Sources and Levels in the Outside Environment*, Indoor Radon and its Hazards, Univ. of Washington Press, 1989, pag. 42-49
9. A.M. Stewart, *Comment on Cohen`s Radon Data and Smoking*, Health Phys., 75 (correspondence), 1998

STUDIA UNIVERSITATIS BABEŞ BOLYAI, PHYSICA, L, 1, 2005

THE INTERNATIONAL INTERCOMPARISON MEASUREMENT OF SOIL-GAS RADON AND RADON EXHALATION RATE FROM THE GROUND AND BUILDING MATERIALS

C. COSMA[1], M. MOLDOVAN[1], D. RISTOIU[1], T. JURCUT[2]

Babes-Bolyai University, Faculty of Environmental Science , Cluj-Napoca
University of Oradea, Department of Sciences, Oradea

ABSTRACT. The International Intercomparison Measurement of Soil-gas Radon Concentration, of Radon Exhalation Rate from Building Materials and of Radon Exhalation Rate from the Ground Surface was held in Pribram, Czech Republic in September 2002. It was attended by participants representing 10 different institutions from 8 countries - France, Germany, Hungary, Poland, Romania, Spain, United Kingdom and Czech Republic. A test site for the intercomparison of soil-gas radon concentration and of radon exhalation from the ground was located in the field, at an area characterized by a high soil permeability and by relatively high values of soil-gas radon concentration. A concrete block made from a slag with a high content of radium was used for the intercomparison of radon exhalation rate from building materials. As for the soil-gas radon concentration and the radon exhalation from the concrete block, a relatively good agreement was observed. The intercomparison differences expressed as a ratio of the standard deviation to the arithmetic mean were about 26 - 28 percent. Substantially larger differences were observed during measurements of radon exhalation rate from the ground surface. The value of the ratio SD/mean was 0.72.

Introduction

This paper describes results of Romanian team (Babes-Bolyai University) to the International Intercomparison Measurement of Soil-gas Radon Concentration, of Radon Exhalation Rate from Building Materials and of Radon Exhalation Rate from the Ground Surface, which was held in Pribram, Czech Republic in September 2002 and organized by RADON v.o.s. corp. The original idea to organize the intercomparison appeared at the ERRICCA 2 kick-off meeting in London in February 2002.

The soil-gas radon (^{222}Rn) concentration **c** (kBq.m^{-3}) is defined as an average radon concentration in the air-filled part of soil-pores in a given volume of soil-gas. Radon exhalation rate **J** (mBq.m^{-2}. s^{-1}) is defined as an average activity of radon emitted from a given surface per unit area and per unit time. First of all, both parameters are used for characterizing the radon potential of soils, but a large range of other applications is known: uranium prospecting, earthquake prediction, risk assessment of waste materials, etc.

It is obvious that from metrological point of view there are many serious problems connected with organizing any field intercomparison measurement of

these parameters. The natural geological environment is almost never homogeneous. The soil-gas radon concentration as well as the radon exhalation rate from the ground may vary, often very greatly, over a small distance, the variations of soil-gas radon with depth are different under changing geological conditions [1-8].

Under these circumstances, values are not reported against a standard or reference measurement. Participants results are simply compared to each other, in order to obtain an indication of the collective precision of various measurements. Geological conditions in a depth of soil-gas sampling as well as conditions on the soil surface should be as homogeneous as possible at the test site. If these requirements are not fulfilled, a large variability of measurement results can be expected. On the other hand, any preliminary measurements should be limited at a chosen test site to avoid a situation that the upper soil layers will remind of a Swiss cheese.

Participants

The intercomparison exercise was attended by participants representing 10 different institutions from 8 countries - France, Germany, Hungary, Poland, Romania, Spain, United Kingdom and Czech Republic. Basic information on the participants is given in Table 1.

Table 1. List of participants

Organization	**Country**	**Representative(s)**
DOSIRAD Company	F	J. Andru
British Geological Survey	U K	J. D. Appleton
National Institute of Nuclear and Biological Protection	Cz	I. Burian, J. Merta
Babes-Bolyai University	Ro	C.Cosma, M.Moldovan
SARAD Environmental Instr.	Ge	S. Feige
Central Mining Institute	Pl	S. Chalupnik, M. Wysocka
Univ. of Mining & Metallurgy	Pl	S. J. Kalita, H. D. Chau
Health Env. Reg. Org. Frederic Joliot-Curie Institute for Radiobiology	Ro H	I. Mocsy Z. Deri, G. Banyasz
University of Cantabria	S	L.S.Quindos Poncela
Radon, v.o.s.	Cz	M. Neznal

Results

Soil-gas radon concentration and radon exhalation rate from the ground surface

The intercomparison exercise of soil-gas radon concentration and of radon exhalation rate was organized in the field at a reference area near the village Buk, less than 10 km from Pribram. The reference site lies 2 km NNE from Milin, 550 m a.s.l., several meters from the road Buk – Radetice, Geological basement is formed by a medium grained biotitic and amphibol-biotitic granodiorite (Milin type) of the Central Bohemian pluton of Paleozoic age. The eluvial granitic material forms the cover [6]. Expected values of soil gas radon concentration are relatively high, soil is highly permeable at the test site. A meadow is on the surface. There is a slight downward gradient to the road Buk - Radetice. At the test site, 12 reference points were marked in a 5x5m grid.

A uniform sampling depth of 0.8 m below the ground surface was recommended for soil-gas radon concentration measurements. The participants were also asked to make several measurements of both parameters in different measuring points and to define the exact locations of their measuring points in the protocol. This approach should enable to decrease the influence of a spatial variability, because not single values, but sets of data would be compared. Last but not least: It was recommended to place the devices for radon exhalation measurements before starting of soil-gas sampling in order to avoid a possibility that an accumulator would be placed on an open hole remaining after soil-gas sampling.

The weather during the intercomparison exercise (September 20, in the afternoon) was variable. It was mostly overcast in the beginning, with some drizzle, and the soil surface was wet. But after one or two hours the sun also appeared.The temperature of air was about 15^{o}C.

The results are shown in Fig.1a. Our laboratory code is (C). The whole set of data consisted of 42 values of soil-gas radon concentration. The spread of all data characterized by the ratio of an arithmetic mean and of a standard deviation was 0.33. Mean values reported by different participants ranged from 77.5 to 213 kBq.m^{-3}, ratios SD/mean from 0.08 to 0.49. If only data sets containing at least 4 values are considered, then the mean values reported by different participants range from 125 to 213 kBq.m^{-3} and the ratios SD/mean from 0.08 to 0.30.

Substantially larger intercomparison differences were observed during measurements of radon exhalation rate from the ground surface, Fig.1b The value of the ratio SD/mean was 0.72. The observed differences among participating laboratories were probably mainly systematic, but available descriptions of measuring methods did not allow any more detailed analysis.

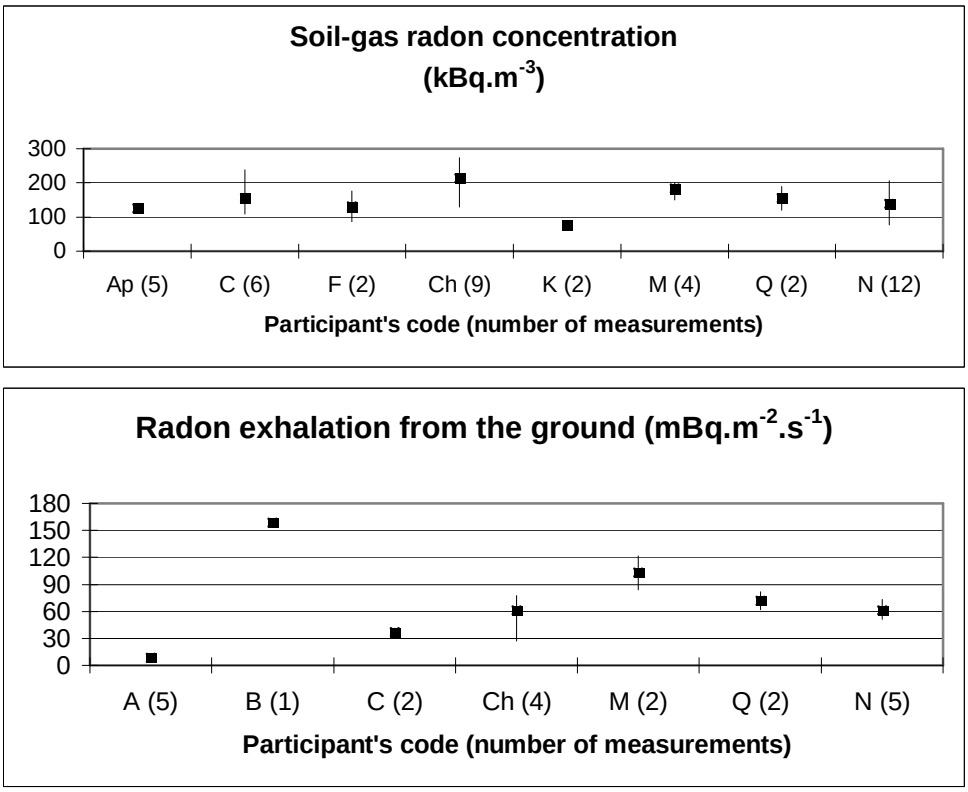

Fig.1. The results of soil radon measurement (upper) and radon exhalation rate (below)

Radon exhalation rate from a concrete block

The intercomparison exercise of this parameter was organized in a dwelling of National Institute of Nuclear, Chemical and Biological Protection near the mine No. 9, Pribram. A concrete block made from a slag with a high content of radium was used (2820 $Bq.kg^{-1}$). As the exhalation rate from the block is not quite homogeneous, 8 different measuring positions were defined. Each position was a circle with a diameter of about 30 cm. Radon exhalation rate from each position had been determined using the same method (RADON, v.o.s.; simple accumulator method) before the intercomparison, on June, 12. These values were then used as a base for the intercomparison, which was held on September, 20, in the morning. The arrangement of measurement devices on the surface of the concrete block is illustrated in Figure 2. Results of measurements of radon exhalation rate are

presented in Figure 3. Five institutions participated in the intercomparison, three of them realized 2 measurements.

This third parameter, that was compared, was the radon exhalation rate from the surface of a concrete block. The spread of original data expressed as a ratio SD/mean was 0.38. Correction factors, which had resulted from preliminary measurements, were then used to minimize the influence of existing spatial variations. Corrected data ranged from 46 to 88 $mBq.m^{-2}.s^{-1}$, the value of SD/mean was 0.26, i.e. the agreement among participants was acceptable.

During the E.M.L. intercomparison exercise in 1995 [4-5], the radon exhalation rate was measured on the surface of an artificially prepared concrete slab with a high content of radium. Identically sized grains and a radium solution were used to get a homogeneous material. Reported values ranged from 81.5 to 490 $mBq.m^{-2}.s^{-1}$, the value of SD/mean was 0.37 (17 measurements; 8 participating laboratories).

Our measurements in Fig.3 are marked also by C code and they are closed to the measurements-N code. The last was considered as reference laboratory.

Fig. 2. The arrangement of measurement devices

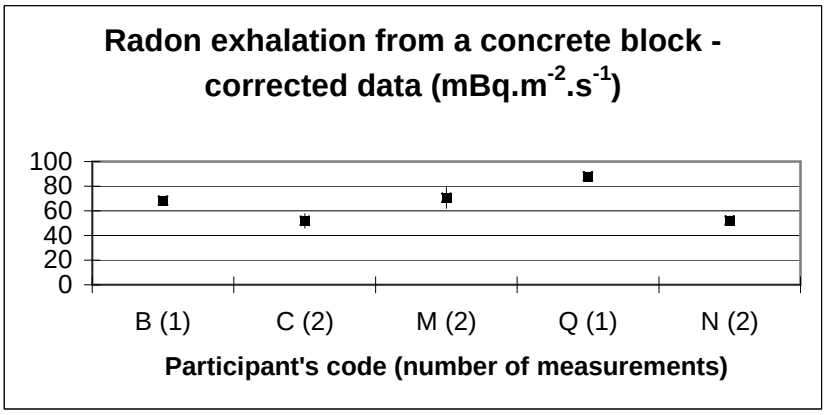

Fig.3. Results of radon exhalation from a concrete block

REFERENCES

1. Cliff, K.D.; Holub, R.F.; Knutson, E.O.; Lettner, H.; Solomon, S.B. International Intercomparison of Measurements of Radon and Radon Decay Products, Badgastein, Austria, September, 29 - 30, 1991. Chilton, Didcot, Oxon. National Radiological Protection Board; 1994
2. Fisenne, I.M. 27th EML Radon Gas Intercomparison. New York: U.S. Department of Energy, Environmental Measurements Laboratory; 1995
3. Hinton, T.G. A Field Experiment on Rn Flux from Reclaimed Uranium Mill Tailings. Health Phys., 48: 421-427; 1985
4. Hutter, A.R.; Knutson, E.O. Report of the Sixth IRPM Intercomparison Test and Workshop: State of the art in measuring soil gas radon and radon exhalation from soil, June 12-15, 1995. New York: U.S. Department of Energy, Environmental Measurements Laboratory; 1996
5. Hutter, A.R.; Knutson, E.O. An International Intercomparison of Soil Gas Radon and Radon Exhalation Measurements. Health Phys., 74: 108-114; 1998
6. Matolin, M. Radon Reference Sites in the Czech Republic. In: Barnet, I.; Neznal, M., eds. Radon Investigations in CR. Vol. 9. Praha: Czech Geological Survey and Radon corp.; 2002: 26-29
7. Neznal, M.; Neznal, M.; Smarda, J. Report on the Intercomparison Measurement of Soil-Gas Radon Concentration and of Radon Exhalation Rate from the Ground, Prague, Czech Republic, September 16, 1996. Lysa nad Labem: Radon, v.o.s.; 1996
8. Neznal, M.; Neznal, M.; Smarda, J. Radon Risk Classification of Foundation Soils - A Five Years Experience. Environ. Int.; 22: S819-S828; 1996
9. Robé, M.C.; Rannou, A.; LeBronec, C. Radon Measurement in the Environment in France. Radiat. Prot. Dosim. 45: 455-457, 1992